Journal of Catalysis 278 (2011) 78–93

Contents lists available at ScienceDirect

Journal of Catalysis

journal homepage: www.elsevier.com/locate/jcat

Catalytic consequences of acid strength in the conversion of methanol to dimethyl ether

Robert T. Carr [a], Matthew Neurock [b], Enrique Iglesia [a,*]

[a] Department of Chemical Engineering, University of California, Berkeley, CA 94720, United States
[b] Departments of Chemical Engineering and Chemistry, University of Virginia, Charlottesville, VA 22904, United States

ARTICLE INFO

Article history:
Received 8 August 2010
Revised 9 November 2010
Accepted 21 November 2010
Available online 3 January 2011

Keywords:
Polyoxometalate
Keggin
Dehydration
Methanol conversion
Density functional theory
Acid strength
Deprotonation energy
BEA

ABSTRACT

The effects of acid identity on CH_3OH dehydration are examined here using density functional theory (DFT) estimates of acid strength (as deprotonation energies, DPE) and reaction energies, combined with rate data on Keggin polyoxometalate (POM) clusters and zeolite H-BEA. Measured first-order (k_{mono}) and zero-order (k_{dimer}) CH_3OH dehydration rate constants depend exponentially on DPE for POM clusters; the value of k_{mono} depends more strongly on DPE than k_{dimer} does. The chemical significance of these rate parameters and the basis for their dependences on acid strength were established by using DFT to estimate the energies of intermediates and transition states involved in elementary steps that are consistent with measured rate equations. We conclude from this treatment that CH_3OH dehydration proceeds via direct reactions of co-adsorbed CH_3OH molecules for relevant solid acids and reaction conditions. Methyl cations formed at ion-pair transition states in these direct routes are solvated by H_2O and CH_3OH more effectively than those in alternate sequential routes involving methoxide formation and subsequent reaction with CH_3OH. The stability of ion-pairs, prevalent as intermediates and transition states on solid acids, depends sensitively on DPE because of concomitant correlations between the stability of the conjugate anionic cluster and DPE. The chemical interpretation of k_{mono} and k_{dimer} from mechanism-based rate equations, together with thermochemical cycles of their respective transition state formations, show that similar charge distributions in the intermediate and transition state involved in k_{dimer} cause its weaker dependence on DPE. Values of k_{mono} involve uncharged reactants and the same ion-pair transition state as k_{dimer}; these species sense acid strength differently and cause the larger effects of DPE on k_{mono}. Confinement effects in H-BEA affect the value of k_{mono} because the different sizes and number of molecules in reactants and transition states selectively stabilize the latter; however, they do not influence k_{dimer}, for which reactants and transition states of similar size sense spatial constraints to the same extent. This combination of theory and experiment for solid acids of known structure sheds considerable light on the relative contributions from solvation, electrostatic and van der Waals interactions in stabilizing cationic transition states and provides predictive insights into the relative contributions of parallel routes based on the size and charge distributions of their relevant intermediates and transition states. These findings also demonstrate how the consequences of acid strength on measured turnover rates depend on reaction conditions and their concomitant changes in the chemical significance of the rate parameters measured. Moreover, the complementary use of experiment and theory in resolving mechanistic controversies has given predictive guidance about how rate and equilibrium constants, often inextricably combined as measured rate parameters, individually depend on acid strength based on the magnitude and spatial distributions of charges in reactants, products and transition states involved in relevant elementary steps. The unique relations between k_{mono}, k_{dimer} and DPE developed here for CH_3OH dehydration can be applied in practice to assess the acid strength of any solid acid, many of which have unknown structures, preventing reliable calculations of their DPE by theory.

1. Introduction

Solid Brønsted acids and the reactions that they catalyze represent some of the most important materials and processes for chemical transformations, specifically those involved in the synthesis and conversion of fuels and chemicals. Active site structures

* Corresponding author.
E-mail addresses: mn4n@virginia.edu (M. Neurock), iglesia@berkeley.edu (E. Iglesia).

0021-9517/$ - see front matter © 2010 Elsevier Inc. All rights reserved.
doi:10.1016/j.jcat.2010.11.017

in solid acids are often non-uniform and inaccessible to direct measurements of their number and acid strength, especially as they exist and evolve during thermal treatment and catalysis. Thus, the elucidation of specific relations among their structure, acid strength, and function remain challenging and often speculative [1]; yet, such insights are essential to improve existing materials and to guide the design of solid acids for specific catalytic purposes.

Tungsten polyoxometalate (POM) clusters with Keggin structure and charge-balancing protons ($H_{8-n}X^{n+}W_{12}O_{40}$) are Brønsted acids with well-defined connectivity and diverse central atoms ($X^{n+} = P^{5+}$, Si^{4+}, Al^{3+}, and Co^{2+}). The central atoms influence their acid strength, but not their Keggin structure, by changing the number of protons and the anionic charge in the conjugate base [2]; as a result, they enable purposeful compositional and functional modifications without concomitant changes in structural motifs. This compositional diversity causes significant changes in deprotonation energies (DPE), which rigorously reflect Brønsted acid strength [3,4]. DPE is the energy required to separate a proton from a conjugate base to non-interacting distances ($AH \rightarrow A^- + H^+$) and can be estimated from quantum mechanical treatments for known structures such as Keggin clusters [2]. Infrared [5] and nuclear magnetic resonance [6] methods and temperature-programmed desorption [7] and microcalorimetry [8] of adsorbed bases can also be used to infer acid strength, but seldom within reaction environments and often with distracting contributions from van der Waals and H-bonding interactions that do not rigorously reflect acid strength. DPE values for Keggin POM clusters decrease (and acid strength increases) as the valence of the central atom increases because of a concomitant increase in the stability of the anionic conjugate cluster. These DPE values range from 1087 kJ mol^{-1} for $H_3PW_{12}O_{40}$ to 1145 kJ mol^{-1} for $H_6CoW_{12}O_{40}$ [2], making these clusters stronger and more diverse acids than zeolites (1171–1200 kJ mol^{-1} DPE for FAU, CHA, MOR, and MFI) [3] or mineral acids, at least as gas-phase monomers (1249 kJ mol^{-1} to 1359 kJ mol^{-1} for $HClO_4$, H_2SO_4, HNO_3, and H_3PO_4) or dimers (1177 kJ mol^{-1} for $H_2S_2O_7$ and 1274 kJ mol^{-1} for $H_4P_2O_7$) [4] in the latter case.

Measured rate constants, derived from mechanistic interpretations of alkanol dehydration and hexane isomerization rates, decreased exponentially with increasing DPE for Keggin POM and zeolite H-BEA acids [2,9,48]. These trends suggest a proportional relation between DPE and kinetically-relevant activation barriers, in which the "correlation strength" reflects the relative electrostatic stabilization of protons and cationic moieties in ion-pairs of late transition states by the anionic conjugate base. These activation barriers can be dissected into contributions from molecular and active site properties using thermochemical cycles [9,48]. These contributions include (i) adsorption of reactants, (ii) deprotonation of the solid acid, (iii) protonation of reactant(s) in the gas-phase, and (iv) interactions between cationic transition states and the conjugate anion. Hexene isomerization barriers depend more strongly on DPE than those for 1-butanol or 2-butanol dehydration because of the more localized charge at transition states involved in the latter reaction, which recover a larger fraction of the energy required to separate the proton from the conjugate base.

These concepts are extended here to CH_3OH dehydration to dimethyl ether (DME), for which dehydration turnovers require bimolecular events, because the C_1 species involved lack stable gas-phase unimolecular dehydration products (in contrast with the C_n alkoxides formed from C_n alkanols). CH_3OH dehydration and its reverse, DME hydration, occur during homologation to hydrocarbons [10] and DME carbonylation/homologation reactions [11,12]. This study resolves long-standing controversies about the mechanism of bimolecular CH_3OH dehydration on solid acid catalysts by combining kinetic data with density functional theory (DFT) calculations. Our results indicate that direct routes, involving reactions between two adsorbed CH_3OH molecules, prevail at all relevant conditions on POM and zeolite acid catalysts. Apparent first- and zero-order rate constants depend differently on DPE values; these differences are explained by the charge distributions of transition states and intermediates involved in their activation barriers. These data and calculations, taken together with previous reports [2,9,48,49], provide predictive guidance for the sensitivity of catalytic reaction rates to acid strength. Mechanistic interpretations of catalytic rates in terms of elementary steps, with rate and equilibrium constants that reflect the chemical properties of the intermediates and transition states involved, are required to rigorously analyze the effects of catalyst composition on function. The effects of DPE on rate constants are consistent with its inclusion in thermochemical descriptions of activation barriers and show that electrostatic stabilization of intermediates and transition states, relative to that of a proton, determines their sensitivity to acid strength. For Brønsted acid catalysis, where ion-pair transition states are a ubiquitous feature, the effects of DPE on activation barriers decrease as the reacting intermediate becomes more charged.

2. Experimental methods

2.1. Catalyst synthesis

$H_3PW_{12}O_{40}$ (Sigma–Aldrich; reagent grade; CAS #12501-23-4), $H_4SiW_{12}O_{40}$ (Aldrich; >99.9%; CAS #12027-43-9), $H_5AlW_{12}O_{40}$ [13], and $H_6CoW_{12}O_{40}$ [14,15] were supported on amorphous SiO_2 (Cab-O-Sil HS-5; 310 m^2 g^{-1}; 1.5 cm^3 g^{-1} pore volume) by incipient wetness impregnation with their respective ethanol solutions (Sigma–Aldrich; >99.5%; anhydrous) at POM surface densities of 0.04 POM nm^{-2}. SiO_2 was washed three times in 1 M HNO_3 and treated in air (UHP Praxair; 0.5 cm^3 g^{-1} s^{-1}) at 573 K for 5 h before impregnation with ethanol solutions of POM (1.5 cm^3 solution g^{-1} SiO_2). Samples were held in closed vials for 24 h after impregnation to ensure uniform distribution of clusters in SiO_2 pores and were then treated in flowing dry air (UHP Praxair; 0.5 cm^3 g^{-1} s^{-1}) at 323 K (0.033 K s^{-1} heating rate) for 24 h.

The MAS-^{31}P-NMR spectra of $H_3PW_{12}O_{40}/SiO_2$ confirmed that the Keggin structure was maintained upon dispersion onto SiO_2 (Supporting information). Transmission electron micrographs showed that POM clusters were present predominantly as isolated clusters on SiO_2 supports (Supporting information). H-BEA (Zeolyst; Si/Al = 11.8) samples were used as received from the manufacturer. Supported Keggin clusters and H-BEA samples were pressed into wafers, crushed, and sieved to retain 125–180 μm aggregates before catalytic and titration measurements.

2.2. Methanol reaction rate measurements

CH_3OH dehydration rates were measured in a differential quartz tubular flow reactor (1.0 cm I.D.) at 373–433 K. Catalyst samples (0.01–0.2 g) were held on a porous quartz disc and heated with a resistive furnace. Temperatures were measured by a thermocouple (Omega K-type; ±0.2 K) held within a dimple at the reactor wall and were controlled electronically (Watlow; Series 982 controller). Catalyst samples were diluted with washed SiO_2 (pressed and sieved to retain 125–180 μm aggregates) to maintain at least 0.1 g of total mass in all experiments to ensure sufficient bed volume for conductive contact with the reactor walls and the thermocouple well. Keggin POM samples were heated to reaction temperature (0.083 K s^{-1} heating rate) in flowing He (UHP Praxair; 0.83 cm^3 s^{-1}) and held for 1 h before catalytic measurements. H-BEA was heated to 773 K (0.083 K s^{-1} heating rate) in dry air (UHP Praxair) and held for 2.5 h before these measurements. All

transfer lines were kept at 393 K to prevent condensation of reactants, products, or titrants. Liquid CH_3OH (Sigma–Aldrich; 99.8%; without additional purification) was mixed with He (UHP Praxair) using a liquid syringe pump (Cole-Palmer 74900 Series). CH_3OH molar flow rates were used to control its partial pressure (0.01–20 kPa) and maintain differential conversions (<10%).

The concentrations of reactants, products, and titrants were determined by gas chromatography using flame ionization detection (Agilent 6890 N GC; 50 m HP-1 column). Dimethyl ether was the only product detected during methanol reactions on all catalysts; products were not detected in empty reactors or in reactors containing washed SiO_2 (0.06 g SiO_2; 1×10^{-5} moles CH_3OH (g SiO_2)$^{-1}$ s^{-1}). Some deactivation was detected (<40% of initial rate after 5 h time on stream) on Keggin POM samples, apparently because of slow CH_3OH homologation and alkene oligomerization reactions. The loss of active sites by intervening deactivation was determined by periodic rate measurements at standard conditions (0.3 kPa CH_3OH) and was used to correct rate data so that turnover frequencies were not influenced by such deactivation.

The number of Brønsted acid sites in each sample was measured by titration with 2,6-di-*tert*-butylpyridine during catalytic CH_3OH reactions to report dehydration rates as accurate turnover rates. Titrant mixtures were prepared by dissolving 2,6-di-*tert*-butylpyridine (Aldrich; >97%; CAS #585-48-8) in CH_3OH (Sigma–Aldrich, 99.8%) to give 9×10^{-5}–1.3×10^{-3} (titrant/CH_3OH) molar ratios. The titrant mixture was introduced into a He gas stream (UHP Praxair) using a syringe pump. Dehydration rates and the number of adsorbed titrant molecules were concurrently measured by gas chromatographic analysis of the reactor effluent using protocols similar to those described earlier. The number of accessible protons (per POM) was determined from the number of titrant molecules (per POM) required to suppress dehydration catalysis, assuming a 1:1 titrant:H^+ adsorption stoichiometry. Pyridine (Aldrich; anhydrous, 99.8%) was also used for titrations of BEA using concentrations and protocols similar to that of hindered pyridine titration.

2.3. Computational methods

Periodic gradient-corrected density functional theory calculations were carried out using the Vienna ab initio Simulation Package (VASP) [16] to determine optimized structures and energies for all stable intermediates and transition states. The wavefunctions were represented by a periodic plane wave basis set expansion (to a cutoff energy of 396.0 eV) and Vanderbilt ultrasoft pseudopotentials described electron-core interactions [17]. Exchange and correlation energies were calculated within the generalized gradient approximation using the Perdew–Wang (PW91) form [18] for the exchange and correlation functional. The full Keggin cluster (1.06 nm in diameter) was modeled by placing it in the center of a $20 \times 20 \times 20$ Å^3 unit cell to provide a vacuum region that prevents electronic interactions between unit cells. A $1 \times 1 \times 1$ Monkhorst–Pack *k*-point mesh was used to sample the first Brillioun zone. All structures were converged until forces on all of the atoms were <0.05 eV Å^{-1}. The electronic structures for each structural optimization step were converged self-consistently to $<1 \times 10^{-4}$ eV.

Transition state structures were calculated by combining the nudged elastic band (NEB) method [19], to approximate transition state structures, with the dimer approach of Henkelman [20], used here to converge and isolate the final transition state structure. Initial reaction trajectories in NEB were determined by linear interpolation among 16 equally spaced images along the reaction coordinate. These images were optimized in the direction perpendicular to the normal vectors connecting images to forces <0.1 eV Å^{-1} to determine minimum energy reaction paths and the transition state structures and energies. NEB transition state structures and trajectories were used as inputs to dimer calculations. The torque on the dimer was minimized at each of its translational steps to <1 eV Å^{-1} or up to 8 times per translation. Dimer calculations were optimized until the forces on all atoms were <0.05 eV Å^{-1} to locate the final transition state.

The optimized $H_3PW_{12}O_{40}$ structure is shown in the Supporting information (Fig. S.3) with the O-atoms and the proton labeled in the local active site used for calculations. Surface structures and transition states for all central atoms were calculated at the same proton (H_{C1}) on a bridging O-atom (O_{C1}). Reaction energies (ΔE_{rxn}) were calculated from the product ($E_{prod,i}$) and reactant energies ($E_{react,j}$) using:

$$\Delta E_{rxn} = \sum_i E_{prod,i} - \sum_j E_{react,j} \quad (1)$$

A similar equation was used for activation barriers, for which the transition state replaces the products in Eq. (1). Reaction and activation energies were not corrected for zero-point vibrational energies (ZPVE) or entropies, because they are computationally prohibitive for full Keggin structures. ZVPE corrections are not expected to influence reported energies because such corrections are similar for reactants and products (or transition states). Deprotonation energies (DPE) for Keggin POM clusters with different central atoms were previously reported [2]. DPE values are defined as the energy required to remove a proton (H^+) from an acid (AH) to distances where interactions with the conjugate base (A^-) are negligible

$$DPE = E_{H+} + E_{A-} - E_{AH} \quad (2)$$

Charges on intermediates and transition states were calculated using Bader charge methods [21,22], which formally distribute the electron density between two atoms along a dividing plane of zero flux. This plane is perpendicular to the chemical bond connecting the two atoms and is located where the charge density is a minimum along the bond.

3. Results and discussion

3.1. Effects of methanol pressure on dehydration turnover rates

Fig. 1 shows measured CH_3OH dehydration turnover rates per accessible H^+ (Table 1) as a function of CH_3OH pressure on Keggin POM clusters ($H_{8-n}X^{n+}W_{12}O_{40}$) with different central atoms (X^{n+} = P^{5+}, Si^{4+}, Al^{3+}, and Co^{2+}) and zeolite H-BEA. Turnover rates initially increased linearly with CH_3OH pressure at all temperatures on all catalysts, but became insensitive to CH_3OH at higher pressures. The shift from linear to zero-order dependence on reactant pressure occurred at higher pressures on Keggin clusters containing central atoms of lower valence (Fig. 1a) and at higher reaction temperatures for a given POM cluster ($H_4SiW_{12}O_{40}$ in Fig. 1b). These rate data are consistent with a Langmuir-type rate expression:

$$r/[H^+] = \frac{\alpha(CH_3OH)}{1 + \beta(CH_3OH)} \quad (3)$$

and with the elementary steps proposed in Section 3.2, which assign specific chemical significance to the kinetic parameters α and β. Accurate values for α and β were estimated by regression of rate data to Eq. (3). The dashed curves in Fig. 1 confirm the accuracy of Eq. (3) in describing all rate data.

Turnover rates are normalized by accessible protons, measured here by titration with 2,6-di-*tert*-butylpyridine during CH_3OH dehydration (Table 1). Titrant molecules are protonated by Brønsted acid sites, making these sites unavailable for CH_3OH dehydration; these titrants cannot coordinate to Lewis acids

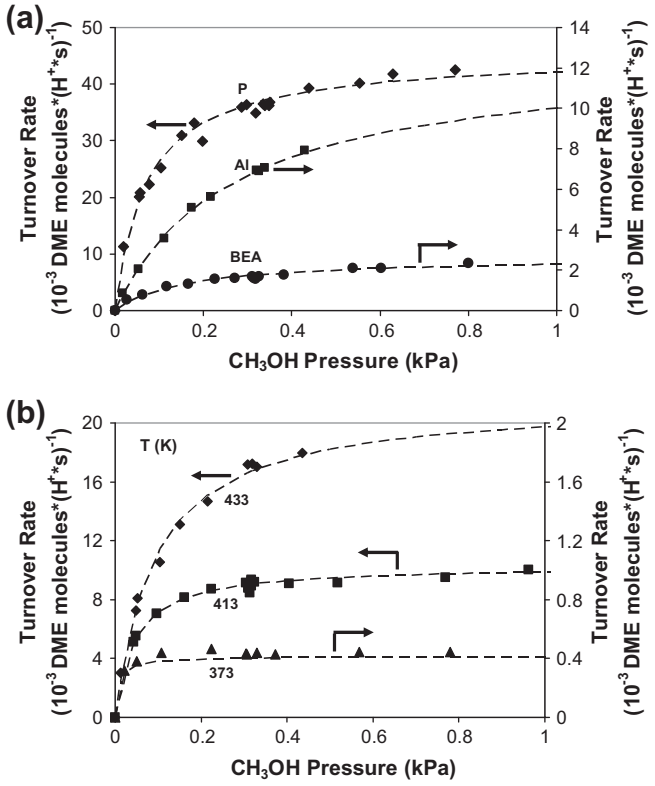

Fig. 1. (a) DME turnover rates (per accessible proton) as a function of CH_3OH pressure at 433 K on $H_3PW_{12}O_{40}/SiO_2$ (♦), $H_5AlW_{12}O_{40}/SiO_2$ (■), and H-BEA (●). Dashed curves represent the regressed best fits to Eq. (3). (b) DME turnover rates (per accessible proton) on $H_4SiW_{12}O_{40}/SiO_2$ as a function of CH_3OH pressure at 373 K (▲), 413 K (■), and 433 K (♦). Dashed curves represent the regressed best fits to Eq. (3).

Table 1
Number of accessible protons per POM cluster or framework Al measured by chemical titration with 2,6-di-*tert*-butylpyridine[a] during CH_3OH dehydration[b] on SiO_2-supported POM clusters and H-BEA zeolite.

Catalyst	POM content (% wt)	POM surface density (nm^{-2})	Accessible H^+ (per POM or framework Al)
$H_3PW_{12}O_{40}$	5	0.04	2.0
$H_4SiW_{12}O_{40}$	5	0.04	3.0
$H_5AlW_{12}O_{40}$	5	0.04	2.3
$H_6CoW_{12}O_{40}$	5	0.04	2.3
H-BEA[c]	–	–	0.55

[a] Assuming a 1:1 titrant:H^+ stoichiometry.
[b] 0.3 kPa CH_3OH, 433 K.
[c] Value listed per framework Al.

because of steric hindrance at their N-atom [23]. In the absence of polar molecules, bulky non-polar titrants cannot penetrate into aggregates of Keggin clusters that form on the support. Polar CH_3OH reactants can expand these agglomerates, however, rendering protons within them accessible to both reactants and titrants.

The number of accessible protons on $H_4SiW_{12}O_{40}$ measured during dehydration catalysis at 413 K was essentially unaffected by CH_3OH pressure (2.3–2.7 H^+/POM, Supporting information), indicating that the effects of reactant pressure (Fig. 1) reflect a kinetic origin instead of concomitant effects of CH_3OH pressure on the accessibility of protons. Fig. 2a shows dehydration rates on $H_4SiW_{12}O_{40}/SiO_2$ at 413 K before and during introduction of hindered pyridine titrants. CH_3OH dehydration rates became undetectable after adsorption of 2.3 hindered pyridine molecules per

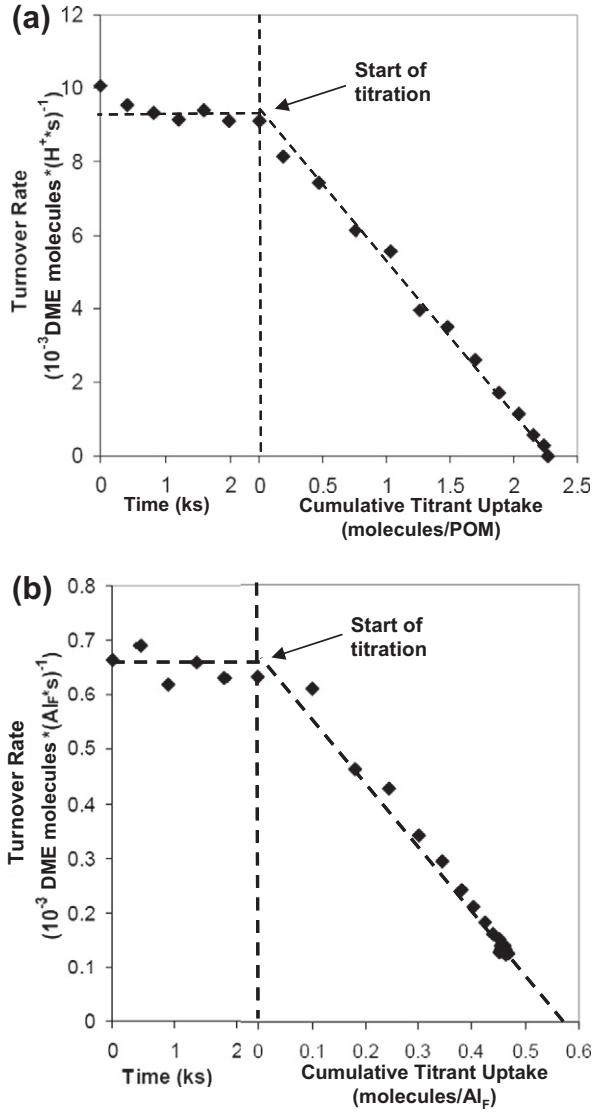

Fig. 2. DME formation turnover rates on (a) $H_4SiW_{12}O_{40}/SiO_2$ at 413 K and (b) H-BEA at 433 K as a function of time before 2,6-di-*tert*-butylpyridine injection (0.3 kPa CH_3OH) and as a function of cumulative titrant uptake (0.3 kPa CH_3OH, 1.4 Pa 2,6-di-*tert*-butylpyridine).

POM, indicating that 2,6-di-*tert*-butylpyridine reaches and titrates all reactive protons during CH_3OH dehydration and that any Lewis acid sites present do not catalyze dehydration at detectable rates.

2,6-di-*tert*-Butylpyridine did not fully suppress CH_3OH dehydration rates on H-BEA (Fig. 2b), and saturation uptakes were less than the number of framework Al atoms (~0.45 titrants per framework Al; measured from ^{27}Al-MAS-NMR, Supporting information). Residual rates after saturation with 2,6-di-*tert*-butylpyridine were much smaller (by a factor of 7) than initial rates and not much different than those measured after saturation with pyridine (0.5 per framework Al; Supporting information), which also titrates Lewis acid sites. Thus, we conclude that Lewis acid sites are not responsible for residual dehydration rates after saturation on H-BEA. Residual rates appear to reflect minority protons that CH_3OH can access, but larger organic bases cannot, in spite of the large three-dimensional channels in BEA. The total number of reactive protons accessible to CH_3OH (Table 1) was measured from the extrapolation of the titration curve in Fig. 2b to zero rates (0.55 H^+ per framework Al); these values are used to calculate the dehydration turnover rates reported here.

3.2. Direct and sequential routes for methanol dehydration on Brønsted acid sites

Next, we consider sequential and direct routes for CH_3OH dehydration on Brønsted acid sites on Keggin POM clusters and BEA in the context of interpreting measured rate data. CH_3OH dehydration has been proposed to occur on acid-form zeolites and Keggin POM via sequential reactions of CH_3OH through methoxide intermediates [24–32] and via a concerted reaction between two adsorbed CH_3OH molecules [33,34]. The sequential route (Scheme 1) involves quasi-equilibrated CH_3OH adsorption through interactions with protons (Step 1) to form CH_3OH "monomers" that eliminate H_2O and form methoxide intermediates (Step 2). A second CH_3OH adsorbs at a vicinal O-atom in another quasi-equilibrated step (Step 3) and the methyl group of the methoxide then transfers to the CH_3OH in a step that reforms the proton as DME desorbs (Steps 4 and 5). In direct dehydration routes (Scheme 2), CH_3OH monomers form by the same path (Step 1), but a second CH_3OH adsorbs and interacts to form protonated dimers before H_2O elimination forms methoxides (Step 2). These dimers then rearrange to co-adsorbed species (Step 3) with the atomic orientation required to form DME and H_2O in a single, subsequent step (Step 4).

The pseudo-steady-state approximation for all adsorbed species, together with quasi-equilibrated CH_3OH adsorption, irreversible H_2O and DME elimination, and sites predominantly occupied by methoxides and CH_3OH monomers in the sequential dehydration route (Scheme 1) give the rate equation (derivation in Supporting information):

$$\frac{r_s}{[H^+]} = \frac{k_{DME,s}K_P(CH_3OH)}{1 + \frac{k_{DME,s}}{k_{elim}}K_P(CH_3OH)} \quad (4)$$

in which k_{elim} and $k_{DME,s}$ are the rate constants for H_2O elimination from monomers (Step 2) and for DME formation from methoxide/CH_3OH pairs (Step 4), respectively, and K_P is the equilibrium constant for CH_3OH adsorption next to methoxide species (Step 3). $[H^+]$ is the number of accessible protons, determined by titration with 2,6-di-*tert*-butyl pyridine during CH_3OH dehydration (Section 3.1 and Table 1). The rate equation for the direct route (Scheme 2) with active sites predominantly occupied by monomers and protonated dimers (derivation in Supporting information) is:

$$\frac{r_d}{[H^+]} = \frac{k_{DME,d}K_CK_D(CH_3OH)}{1 + K_D(CH_3OH)} \quad (5)$$

in which $k_{DME,d}$ is the rate constant for DME formation from co-adsorbed species (Step 4), and K_D and K_C are the adsorption equilibrium constants for protonated dimers (Step 2) and co-adsorbed species (Step 3), respectively. These treatments give rate equations for the two routes that differ only in the chemical significance of their respective rate parameters; both are consistent with the measured effects of CH_3OH pressure on dehydration rates (Fig. 1 and Eq. (3)). The involvement of these mechanisms can only be discerned by comparing rate and equilibrium constants estimated from the energies of intermediates and transition states derived from DFT calculations.

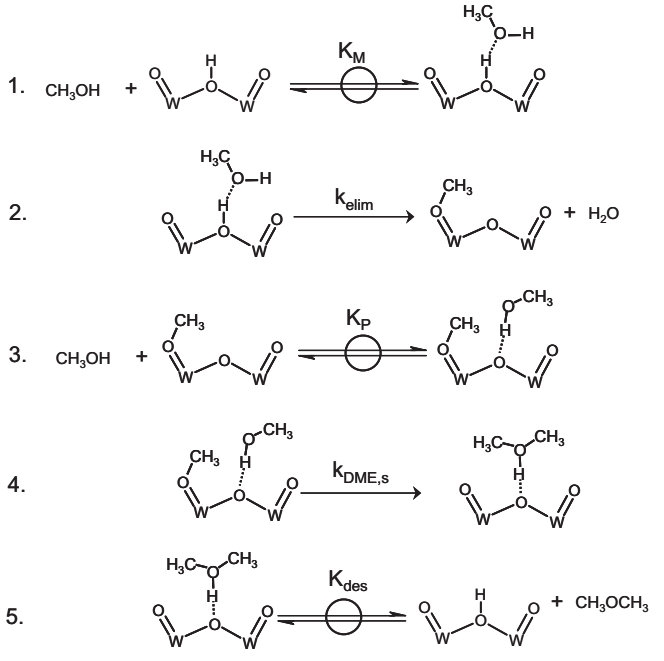

Scheme 1. Elementary steps in the sequential CH_3OH dehydration route. Dashed lines represent H-bonding interactions.

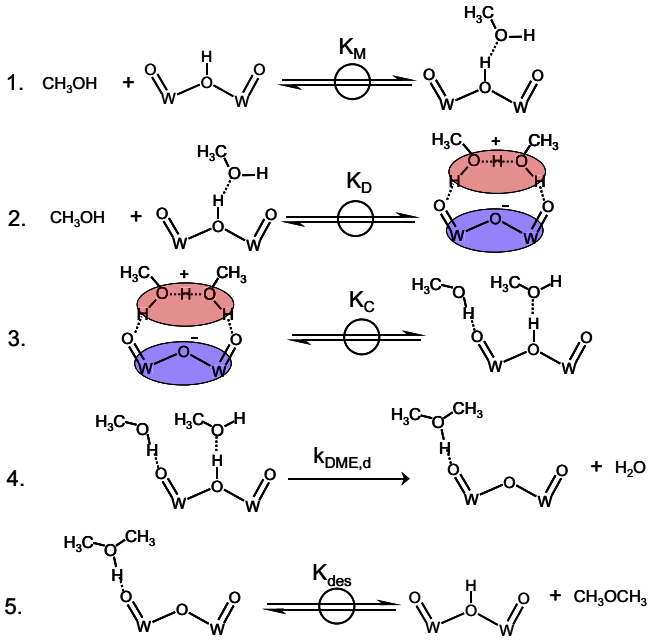

Scheme 2. Elementary steps in the direct CH_3OH dehydration route. Dashed lines represent H-bonding interactions.

3.3. Energies for reaction intermediates and transition states on Keggin POM from density functional theory

Optimized energies and structures of intermediates and transition states in the sequential and direct routes were calculated for Keggin POM clusters with different central atoms (S, P, Si, Al, Co) and are shown in Fig. 3a and b on $H_3PW_{12}O_{40}$, respectively. Keggin clusters with sulfur central atoms were calculated, even though they have not been synthesized in their proton form, so as to examine the catalytic consequences of composition and acid strength over the widest possible range. Corresponding energies for intermediates and transition states on H-BEA were not calculated because they strongly depend on van der Waals forces unrelated to acid strength (or DPE values) and require higher-level theoretical treatments that are computationally prohibitive for these systems [58]. The effects of these additional forces are examined later in Section 3.5 by comparing measured rate constants on H-BEA and Keggin POM clusters. The optimized bond lengths and Bader charges for all of the intermediates and transition states on the different Keggin POM clusters are reported in Tables 2 and 3. Table 4

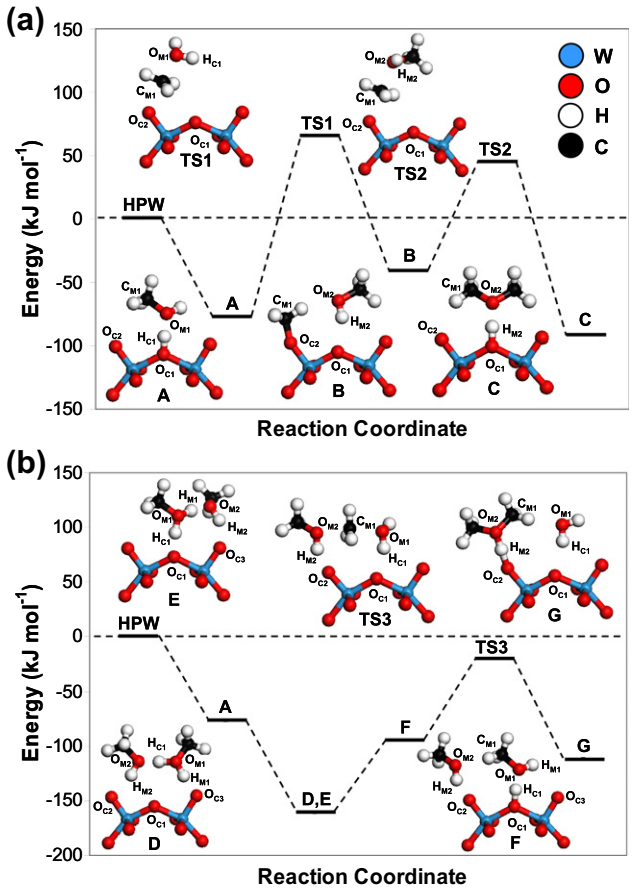

Fig. 3. Structures and energies of intermediates and transition states calculated for (a) the sequential route and (b) the direct route on $H_3PW_{12}O_{40}$. Atomic labels correspond to those used to report the distances listed in Tables 2 and 3 for the sequential and direct routes, respectively. Atomic colors correspond to elemental identity (blue = W, red = O, white = H, black = C). (For interpretation of the references to color in this figure legend, the reader is referred to the web version of this article.)

shows energies for all intermediates and transition states relative to two gas-phase CH_3OH molecules and a bare POM cluster. The energies of selected intermediates and of all transition states on POM clusters are shown in Figs. 4 and 5, respectively, as a function of calculated DPE values.

3.3.1. Formation of adsorbed methanol monomers

Both routes share the initial adsorption of CH_3OH at protons located on bridging O-atoms in POM clusters to form monomers (A in Fig. 3a). Monomers at terminal O-atoms were less favorable than on bridging O-atoms by 11 kJ mol^{-1} (Supporting information). Previous calculations on $H_3PW_{12}O_{40}$ showed that H_2O and CH_3OH assist "proton-hopping" which greatly increases surface mobility [35] so that protons and monomers reach their equilibrium locations (a bridging to terminal ratio of 20 at 433 K for monomers). The adsorbed CH_3OH structures resemble those proposed for CH_3OH-proton adducts from theoretical [29,31], NMR [36,37] and infrared [25,26,38] evidence. The O-atom in CH_3OH (O_{M1}) is oriented toward the Keggin proton (H_{C1}) and its H-atom (H_{M1}) points toward a vicinal terminal O-atom (O_{C3}). The O_{C1}–O_{M1} distance (0.247 nm) for CH_3OH adsorbed on $H_3PW_{12}O_{40}$, is shorter than for H-bonds among H_2O (0.276 nm) or alkanol (0.274 nm) molecules [39,40]. The H_{C1}–O_{C1} distances (0.107 nm) are similar to those in non-interacting protonated POM clusters (0.097 nm), and the POM proton remains closer to O_{C1} than O_{M1} indicating that

Table 2
Atomic distances (listed in nm) and Bader charges (listed as electron charges) of intermediates and transition states in the sequential route for CH_3OH dehydration (Scheme 1).

Species[a]	Central atom				
	S	P	Si	Al	Co
Bare cluster					
H_{C1}–O_{C1}	0.098	0.097	0.097	0.097	0.097
Monomer (A)					
H_{C1}–O_{C1}	0.108	0.107	0.107	0.108	0.104
H_{C1}–O_{M1}	0.141	0.140	0.140	0.139	0.149
C_{M1}–O_{M1}	0.146	0.146	0.146	0.146	0.145
C_{M1}–O_{C2}	0.324	0.333	0.326	0.337	0.350
H_{C1} Bader charge	0.730	0.730	0.644	0.662	0.750
CH_3OH Bader charge	0.000	0.116	0.000	0.084	0.089
H_2O elimination TS (TS1)					
H_{C1}–O_{C1}	0.404	0.398	0.367	0.371	0.182
H_{C1}–O_{M1}	0.098	0.098	0.098	0.098	0.099
C_{M1}–O_{M1}	0.186	0.184	0.183	0.181	0.253
C_{M1}–O_{C2}	0.207	0.208	0.210	0.213	0.250
Methyl Bader charge	0.580	0.590	0.590	0.580	0.596
Water Bader charge	0.190	0.200	0.230	0.210	0.250
Methoxide/CH_3OH pairs (B)					
H_{M2}–O_{C1}	0.205	0.204	0.201	0.213	0.208
H_{M2}–O_{M2}	0.097	0.098	0.098	0.097	0.097
C_{M1}–O_{M2}	0.317	0.327	0.320	0.327	0.331
C_{M1}–O_{C2}	0.144	0.143	0.143	0.143	0.142
DME formation TS (TS2)					
H_{M2}–O_{C1}	0.473	0.470	0.482	0.395	0.208
H_{M2}–O_{M2}	0.098	0.098	0.098	0.098	0.099
C_{M1}–O_{M2}	0.193	0.192	0.189	0.189	0.202
C_{M1}–O_{C2}	0.199	0.200	0.201	0.203	0.205
Methyl Bader charge	0.571	0.570	0.570	0.570	0.560
CH_3OH Bader charge	0.221	0.190	0.230	0.200	0.200
Adsorbed DME (C)					
C_{M1}–O_{M2}	0.144	0.145	0.144	0.144	0.144
C_{M1}–O_{C2}	0.323	0.323	0.323	0.329	0.324

[a] Atomic and structural labels correspond to diagrams in Fig. 3a.

protons are not transferred to the adsorbed CH_3OH. Protonated CH_3OH ions (i.e. methyl-oxonium cations $[CH_3OH_2]^+$) relaxed to adsorbed monomers (A in Fig. 3a) during structure optimization calculations, indicating that the cations are unstable compared to less charged monomer species. $[CH_3OH_2]^+$ ions could only be calculated as transition states in CH_3OH-assisted proton-hopping reactions. The activation barrier for this reaction, which is measured from uncharged monomers, is 15 kJ mol^{-1} on $H_3PW_{12}O_{40}$ (Supporting information) and indicates that proton transfer to form $[CH_3OH_2]^+$ ions is endothermic.

CH_3OH adsorption energies on Keggin clusters ranged from −62 kJ mol^{-1} to −75 kJ mol^{-1} (Table 4 and Fig. 4), indicative of strong interactions between CH_3OH and protons as a result of the partial charge on H_{C1} (+0.64 to +0.75 e Bader charge). These electrostatic interactions stabilize monomers more effectively than typical intermolecular H-bonds in gaseous H_2O and CH_3OH (18–21 kJ mol^{-1} and 13–31 kJ mol^{-1}, respectively) [41–43]. CH_3OH monomers become less stable with increasing DPE (Fig. 4) because the partial charges on protons, needed for strong adsorption, become less stable on weaker acids. CH_3OH adsorption energies are similar on Keggin clusters and aluminosilicate structures in large-pore zeolites (−63 to −73 kJ mol^{-1}) [33,31,44] even though POM clusters are stronger acids, possibly because zeolite frameworks provide additional van der Waals stabilization unrelated to acid strength or DPE.

DME formation from strongly H-bonded CH_3OH species proceeds via the two routes described earlier (Schemes 1 and 2). The sequential path involves the elimination of H_2O to form a methoxide (Scheme 1, Step 2) that subsequently reacts with another

Table 3
Atomic distances (listed in nm) and Bader charges (listed as electron charges) of intermediates and transition states in the direct route for CH_3OH dehydration (Scheme 2).

Species[a]	Central atom				
	S	P	Si	Al	Co
Protonated dimer D (D)					
H_{C1}–O_{C1}	0.295	0.284	0.275	0.271	0.267
H_{M1}–O_{C3}	0.162	0.154	0.160	0.157	0.148
H_{M2}–O_{C2}	0.173	0.187	0.179	0.181	0.185
Dimer Bader charge	0.882	0.875	0.876	0.869	0.856
Protonated dimer E (E)					
H_{C1}–O_{C1}	0.158	0.148	0.148	0.150	0.139
H_{C1}–O_{M1}	0.103	0.105	0.104	0.104	0.108
H_{M2}–O_{C3}	0.175	0.184	0.177	0.169	0.176
Dimer Bader charge	0.883	0.871	0.866	0.856	0.838
Co-adsorbed CH_3OH (F)					
H_{C1}–O_{C1}	0.112	0.110	0.110	0.108	0.105
H_{C1}–O_{M1}	0.132	0.134	0.134	0.139	0.144
C_{M1}–O_{M1}	0.147	0.146	0.146	0.146	0.146
C_{M1}–O_{M2}	0.295	0.326	0.289	0.312	0.327
DME formation TS (TS3)					
H_{C1}–O_{C1}	0.181	0.188	0.180	0.170	0.171
H_{C1}–O_{M1}	0.100	0.099	0.100	0.101	0.101
C_{M1}–O_{M1}	0.193	0.193	0.192	0.193	0.195
C_{M1}–O_{M2}	0.200	0.201	0.199	0.198	0.198
Methyl Bader charge	0.561	0.559	0.546	0.541	0.538
Water Bader charge	0.170	0.181	0.181	0.171	0.168
CH_3OH Bader charge	0.180	0.169	0.171	0.181	0.178
Adsorbed DME + H_2O (G)					
H_{C1}–O_{C1}	0.219	0.211	0.219	0.212	0.209
H_{C1}–O_{M1}	0.098	0.098	0.098	0.098	0.098
H_{M2}–O_{C2}	0.130	0.125	0.119	0.115	0.110
C_{M1}–O_{M1}	0.305	0.302	0.306	0.319	0.312
C_{M1}–O_{M2}	0.147	0.147	0.146	0.146	0.145

[a] Atomic and structural labels correspond to diagrams in Fig. 3b.

Table 4
Energies (in kJ mol^{-1}) of intermediates and transition states relative to non-interacting clusters and two gas-phase CH_3OH in CH_3OH dehydration for sequential (Scheme 1) and direct (Scheme 2) routes.

Species[a]	POM central atom				
	S	P	Si	Al	Co
Bare cluster	0.0	0.0	0.0	0.0	0.0
Monomer (A)	−72.5	−74.6	−66.4	−63.5	−61.7
Sequential route					
H_2O Elimination TS (TS1)	66.9	68.8	77.7	76.9	104.6
Methoxide + H_2O_{ads}	−31.2	−36.6	−39.6	−39.4	−41.1
Methoxide	−10.4	−17.1	−19.2	−15.5	−18.1
Methoxide/CH_3OH pairs (B)	−23.6	−34.5	−35.9	−35.9	−34.3
DME formation TS (TS2)	49.3	50.9	53.5	63.9	84.3
Adsorbed DME (C)	−85.4	−85.2	−84.9	−81.2	−75.8
Direct route					
Protonated dimer D (D)	−155.3	−155.1	−143.6	−134.5	−123.2
Protonated dimer E (E)	−155.2	−153.9	−147.6	−140.5	−130.6
Co-adsorbed CH_3OH (F)	−88.5	−88.7	−87.6	−99.5	−82.8
DME formation TS (TS3)	−17.3	−13.7	−10.2	0.0	12.9
Adsorbed DME + H_2O (G)	−113.1	−105.3	−104.6	−107.3	−91.1

[a] Structural labels correspond to diagrams in Fig. 3.

CH_3OH molecule to form DME (Scheme 1, Step 4) and restore the proton. The direct route involves a bimolecular reaction between two adsorbed CH_3OH molecules to eliminate H_2O and to form protonated DME (Scheme 2, Step 4) simultaneously. These routes are examined separately next by calculating the structures and energies of their respective transition states and intermediates on Keggin POM with different central atoms (S, P, Si, Al, Co).

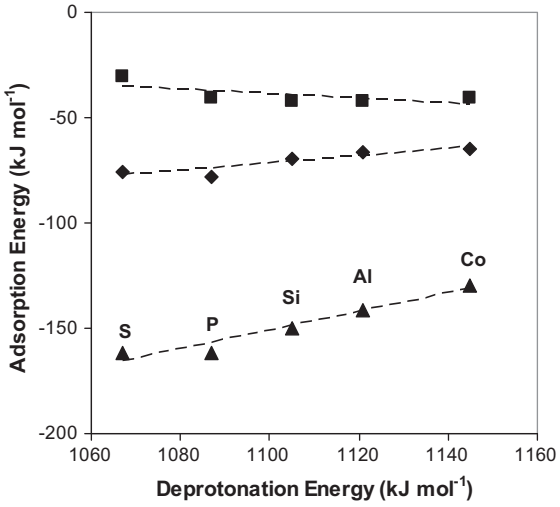

Fig. 4. Calculated adsorption energies for monomers (A in Fig. 3a, ♦), methoxide/CH_3OH pairs (B in Fig. 3a, ■), and protonated dimers (D in Fig. 3b, ▲) on $H_{8-n}X^{n+}W_{12}O_{40}$ (X = S, P, Si, Al, Co) clusters as a function of deprotonation energies. Adsorption energy values are relative to bare clusters and two gas-phase CH_3OH molecules. Dashed lines are linear best fits of the calculated values.

3.3.2. Methanol dehydration by the sequential route

The first step in the sequential route is H_2O elimination from monomers, forming covalently bound methoxides (Scheme 1, Step 2). The chemical outcome and the structures along this reaction coordinate are reminiscent of S_N2 reactions in which the POM O-atom (O_{C2}) acts as the nucleophile, H_2O as the leaving group, and the methyl group as the electrophile. The transition state (shown for $H_3PW_{12}O_{40}$ in Fig. 3a as TS1) involves the transfer of the proton from the POM cluster to the O-atom in adsorbed CH_3OH (H_{C1}–O_{C1} = 0.398 nm and H_{C1}–O_{M1} = 0.098 nm at TS1 vs. 0.107 nm and 0.140 nm, respectively, in monomers) with the simultaneous elongation and cleavage of the C–O bond in CH_3OH (C_{M1}–O_{M1} = 0.184 nm at TS1 vs. 0.146 nm in the monomer) to form H_2O. The O-atom in the H_2O, the methyl species, and the terminal O-atom of the POM (O_{C2}) are arranged in a straight line at the transition state, consistent with the arrangement required for the proper alignment of orbitals in S_N2-type reactions [45]. The umbrella-like methyl in CH_3OH must invert upon methoxide formation as a planar methyl cation at the transition state (TS1 in Fig. 3a). Bader charges in the POM cluster (−0.79 e), methyl (+0.59 e), and H_2O (+0.20 e) fragments indicate that this is a late ion-pair transition state with the methyl cation stabilized by ion–dipole contact with the H_2O molecule and by electrostatic interactions with neighboring O-atoms in the anionic POM cluster (O_{C2} and O_{C1}).

The corresponding transition state energy relative to gas-phase CH_3OH is 69 kJ mol^{-1} on $H_3PW_{12}O_{40}$ and increases weakly with increasing DPE (Fig. 5a), because charge separation at the ion-pair transition state requires more energy on weaker acids. The transition state energy for this step on $H_6CoW_{12}O_{40}$ lies above the trend defined by the other POM clusters because it occurs earlier along the reaction coordinate, as shown by its bent configuration, which contrasts the linear structures found for other POM clusters (Fig. 6). The conjugate anion stabilizes the cationic charge on H_2O (+0.25 e) more effectively in this bent conformation than in linear structures because of smaller distances between charged moieties, but it has inappropriate atomic positions for S_N2 reactions. As charge separation becomes more costly on weaker acids, H_2O elimination transition states occur earlier along the reaction coordinate to retain the H_2O fragment near the anionic cluster, but will involve increasingly unstable structures that cannot align their molecular orbitals for S_N2 reactions.

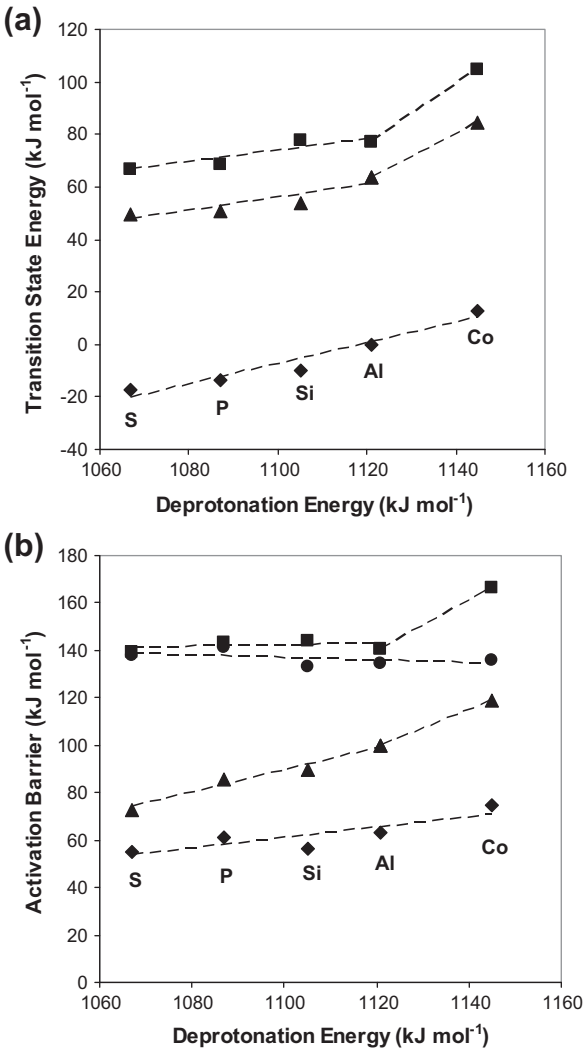

Fig. 5. (a) Calculated transition state energies relative to two gas-phase CH_3OH for sequential H_2O elimination (TS1 in Fig. 3a, ■), sequential DME formation (TS2 in Fig. 3a, ▲), and direct DME formation (TS3 in Fig. 3b, ♦) on $H_{8-n}X^{n+}W_{12}O_{40}$ (X = S, P, Si, Al, Co) clusters as a function of deprotonation energy. Dashed lines are linear best fits of the calculated values. (b) Calculated activation barriers for sequential H_2O elimination from monomers (TS1 in Fig. 3a, ■), sequential DME formation from methoxide/CH_3OH pairs (TS2 in Fig. 3a, ▲), direct DME formation from monomers and gas-phase CH_3OH (TS3 in Fig. 3b, ♦), and direct DME formation from protonated dimers (TS3 in Fig. 3b, ●) on $H_{8-n}X^{n+}W_{12}O_{40}$ (X = S, P, Si, Al, Co) clusters as a function of deprotonation energy. Dashed lines are linear best fits of the calculated values.

The activation barriers for H_2O elimination (Fig. 5b) from monomers (A in Fig. 3a) are significantly higher than their respective transition state energies (measured with respect to gas-phase CH_3OH). They only depend weakly on DPE (140 kJ mol^{-1} except for $H_6CoW_{12}O_{40}$ for the reasons earlier), because DPE effects on transition state and the monomer energies nearly cancel out. These high barriers for H_2O elimination reflect the unstable nature of methyl cations; they are, however, much smaller than for dehydration of gaseous methyl-oxonium ions (i.e. $[CH_3OH_2]^+_{(g)} \rightarrow CH^+_{3(g)} + H_2O_{(g)}$; E_{dehy} = 290 kJ mol^{-1}) [46,51] because electrostatic stabilization by the anionic cluster and ion–dipole interactions with the neighboring H_2O molecule stabilize methyl ions at the elimination transition state. Blaszkowski and van Santen calculated an activation barrier of 215 kJ mol^{-1} for methoxide formation on a small aluminosilicate cluster [34]. This value is significantly higher than the values calculated on POM clusters here, possibly because of the lack of charge screening on small zeolite clusters [47]. H_2O loses its charge upon methoxide formation (−0.01 e Bader charge; Supporting information) and desorbs subsequently in an endothermic step (19–24 kJ mol^{-1}), whose reaction energy does not depend on the DPE of the POM cluster (Table 4).

The transition state involved in H_2O elimination from CH_3OH monomers (TS1) resembles that for H_2O elimination from larger H-bonded alkanols on POM clusters [48,49] and is consistent with the ubiquitous involvement of late ion-pairs at transition states for Brønsted acid catalysis [9,48]. Both transition states have full proton transfer to the alkanol and cleavage of the alkanol C–O bond to form H_2O interacting with planar carbenium cations. Elimination barriers for CH_3OH (139 to 144 kJ mol^{-1} for all POM clusters) are similar to previous estimates for 2-butanol elimination (127–146 kJ mol^{-1}) [49] on POM clusters. Thermochemical cycles (discussed in Section 3.5 and shown for the comparison of CH_3OH and butanol activation barriers in the Supporting information) show that the similar activation barriers for CH_3OH and 2-butanol dehydration (for a given acid) reflect compensation between (i) gas-phase alkanol dehydration energies (E_{dehy}; $ROH_{(g)} + H^+_{(g)} \rightarrow R^+_{(g)} + H_2O_{(g)}$), (ii) stabilization of the gas-phase carbenium ion (R^+) by H_2O at the gas-phase transition state analog (E_{water}), and (iii) electrostatic stabilization of this gas-phase analog by the anionic cluster ($E_{ES,POM}$):

$$E_{a,MeOH} - E_{a,BuOH} = (E_{dehy} + E_{water} + E_{ES,POM})_{MeOH} - (E_{dehy} + E_{water} + E_{ES,POM})_{BuOH} \quad (6)$$

Gas-phase 2-butanol dehydration is much more exothermic (E_{dehy} = −720 kJ mol^{-1}) than for CH_3OH (E_{dehy} = −485 kJ mol^{-1}) [51,46], because alkyl induction effects stabilize butyl cations. These differences are attenuated, however, by stronger stabilization of methyl cations than butyl cations by H_2O and the conjugate anion (detailed calculations in Supporting information) [49,50]. The distance between the planar C-atom and the O-atom in the eliminated H_2O for TS1 (O_{M1}–C_{M1} = 0.184 nm) is 0.07 nm shorter than in the 2-butanol dehydration transition state (0.26 nm) [49], and as such, methyl cations coordinate more strongly with H_2O to form a carbenium–water complex. Similar activation barriers for H_2O elimination from CH_3OH and 2-butanol, even though butyl cations are much more stable than methyl cations, indicate that the stabilization of methyl groups at CH_3OH transition states is essential for low CH_3OH dehydration activation barriers. These findings suggest, in turn, that routes that do so more effectively, such as the direct dehydration route, may circumvent the high energy barriers associated with the sequential formation and reaction of methoxide intermediates.

Adsorption of a second CH_3OH molecule at a bridging O-atom (O_{C1}), vicinal to a methoxide, leads to methoxide/CH_3OH pairs (Scheme 1, Step 3) that form DME by methyl transfer. The hydroxyl H-atom (H_{M2}) of the adsorbed CH_3OH interacts with a bridging POM O-atom (O_{C1}), while its O-atom (O_{M2}) interacts with the C-atom in the methoxide (B in Fig. 3a). The adsorption energy of this second CH_3OH (−16 to −24 kJ mol^{-1}; Table 4) is typical of a H-bond and is weaker than the adsorption of the first CH_3OH at POM protons to form monomers (−75 to −62 kJ mol^{-1}; Table 4) because of the absence of electrostatic stabilization. The O-atom separation in this H-bond (O_{M2}–O_{C1} = 0.298 nm on $H_3PW_{12}O_{40}$) is longer than in solid H_2O (0.276 nm) [40] and binding energies resemble those among gas-phase CH_3OH molecules (13 to 30 kJ mol^{-1}) [42,43]. These methoxide/CH_3OH pairs react via nucleophilic attack of the methyl by CH_3OH to form DME (Scheme 1, Step 4) in a step that resembles the reverse of H_2O elimination (Scheme 1, Step 2), except that CH_3OH is present instead of H_2O. The C_{M1}–O_{M2} distance (0.317–0.331 nm; Table 2) in methoxide/CH_3OH pairs shortens as DME forms (C in Fig. 3a, C_{M1}–O_{M2} = 0.145 nm). The transition state (TS2 in Fig. 3a) consists

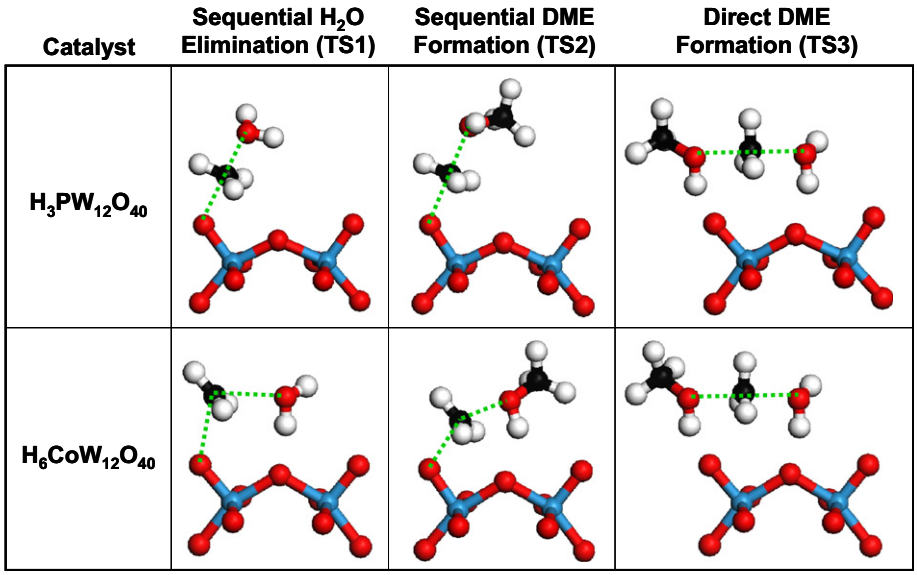

Fig. 6. Structures of transition states involved in sequential and direct paths of CH_3OH dehydration on $H_3PW_{12}O_{40}$ and $H_6CoW_{12}O_{40}$ clusters. All transition states on $H_3PW_{12}O_{40}$ and the direct DME formation transition state on $H_6CoW_{12}O_{40}$ have methyl cations arranged in linear structures (shown by the dotted lines) appropriate for S_N2 reactions. Transition states for the sequential route on $H_6CoW_{12}O_{40}$ have methyl cations in bent conformations (shown by the dotted lines).

of a planar methyl (+0.57 e Bader charge) stabilized by the O-atom in CH_3OH (+0.20 e Bader charge and O_{M2}–C_{M1} = 0.192 nm) and POM clusters (O_{C2}–C_{M1} = 0.200 nm). Similar to the H_2O elimination transition state, the terminal POM O-atom, methyl, and CH_3OH O-atom are in a linear arrangement that is conducive to S_N2 substitution for all POM central atoms except $H_6CoW_{12}O_{40}$ (Fig. 6).

The transition state energies to form DME (with respect to two gas-phase CH_3OH) increase slightly with increasing DPE (Fig. 5a), as in the case of H_2O elimination from CH_3OH monomers. They are consistently smaller, however, because CH_3OH stabilizes cationic methyl fragments via ion–dipole interactions more effectively than H_2O (Scheme 3, Supporting information). DME formation activation barriers (85 kJ mol^{-1} on $H_3PW_{12}O_{40}$), measured with respect to methoxide/CH_3OH pairs, are significantly smaller than for H_2O elimination from monomers (Fig. 5b), predominantly because methoxide/CH_3OH pairs (and gas-phase H_2O) involved in DME formation are less stable than the monomers (and gas-phase CH_3OH) that precede H_2O elimination (Fig. 3a). This sequential CH_3OH dehydration catalytic sequence is completed by desorption of DME and the re-protonation of the POM cluster (Scheme 1, Step 5), in a concerted step with reaction energies of 65–75 kJ mol^{-1} for these POM clusters (Table 4).

3.3.3. Direct route for methanol conversion to dimethyl ether

Direct CH_3OH dehydration routes involve reactions of gas-phase CH_3OH with monomers to form adsorbed dimers (Scheme 2, Step 2); these dimers are stabilized by concerted interactions among POM protons, OH groups in the two CH_3OH molecules, and vicinal

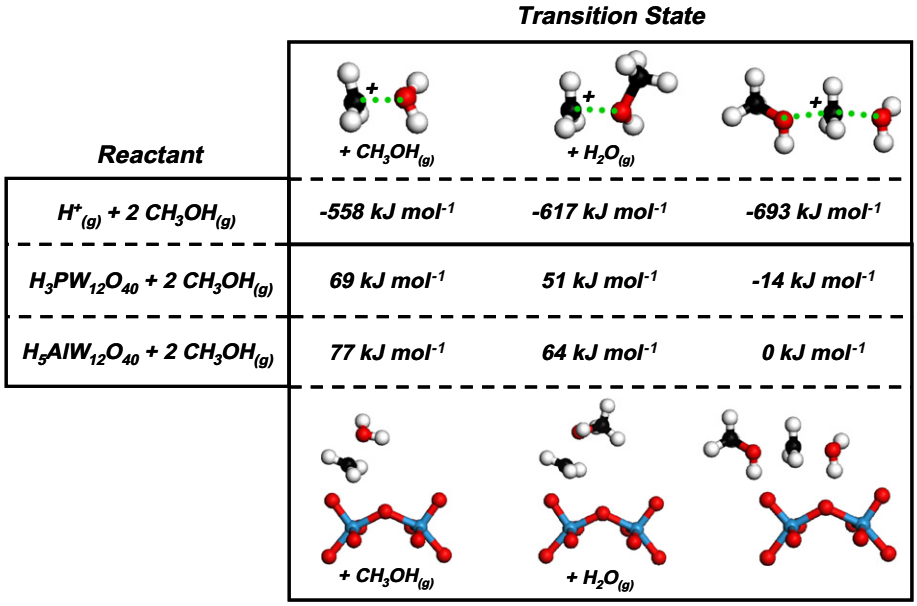

Scheme 3. Energies and structures of transition states and their gas-phase analogs in sequential and direct dehydration routes. Energies of transition states are reported relative to two gas-phase CH_3OH and the bare acid (or a gas-phase proton for the gas-phase transition states). Energies decrease in the order: sequential H_2O elimination, sequential DME formation, and direct DME formation for all cases.

POM O-atoms. The two most stable dimers investigated are shown as D and E in Fig. 3b. In "dimer D", the proton lies between the O-atoms in the two CH_3OH molecules and each CH_3OH molecule acts as a H-bond donor to a vicinal terminal O-atom in the POM cluster (O_{C2} and O_{C3}). The H_{C1}–O_{C1} distance (0.295–0.267 nm vs. 0.097 nm in unreacted POM clusters) is consistent with significant proton transfer in these dimer structures, a conclusion also confirmed by their Bader charges (+0.88 to +0.86 e); thus, we denote these species as protonated dimers. The adsorption energy for this protonated dimer, relative to its CH_3OH monomer and gas-phase CH_3OH precursors, is −85 kJ mol^{-1} on $H_3PW_{12}O_{40}$. This large negative value reflects charge separation in dimers that provides electrostatic stabilization to bind dimers to POM clusters more strongly than H-bonds among CH_3OH (−13 to −30 kJ mol^{-1}) [42,43]. Dimers are more stable as DPE decreases because charge separation is less costly for stronger acids. Dimer formation energies (relative to two gas-phase CH_3OH) are more sensitive to DPE than those for less charged CH_3OH monomers (Fig. 4).

The other stable dimer structure (E in Fig. 3b) orients the H-atom in the monomer (H_{M1}) directly toward the O-atom in the other CH_3OH (O_{M2}), which itself is H-bonded to a vicinal terminal POM O-atom (O_{C3}) through its H-atom (H_{M2}). The H_{C1}–O_{M1} (0.105 nm) and H_{C1}–O_{C1} (0.148 nm) distances and Bader charges (+0.88 to +0.84 e) are also consistent with nearly complete transfer of POM protons to CH_3OH molecules. The formation energies are consequently similar for dimers D and E (−83 kJ mol^{-1} vs. −85 kJ mol^{-1} on $H_3PW_{12}O_{40}$). DPE effects on stability are slightly weaker for E than D structures (Table 4), but both structures are much more sensitive to DPE than monomers. The small energy differences between the two dimers for each POM cluster (<10 kJ mol^{-1}; Table 4) indicate that they co-exist during steady-state CH_3OH dehydration catalysis.

DME formation from protonated dimers requires that the methyl in one CH_3OH molecule approach the O-atom of the other CH_3OH molecule; this requires significant rearrangements of these dimers, in which the two OH groups face each other and the methyl groups point away from each other (D and E in Fig. 3b). As a result, dimers must first reorient to a structure, denoted here as the "co-adsorbed state" (F in Fig. 3b), which resembles a CH_3OH monomer interacting weakly with a CH_3OH that is H-bonded to a vicinal terminal POM O-atom (O_{C2}). The monomer methyl group interacts with the O-atom in the other CH_3OH (C_{M1}–O_{M2} = 0.289–0.327 nm; Table 3) in a configuration that becomes geometrically conducive to methyl transfer. The proton is not transferred from the POM to the co-adsorbed CH_3OH (H_{C1}–O_{C1} = 0.112–0.105 nm and H_{C1}–O_{M1} = 0.132 to 0.144 nm; +0.12 e Bader charge); thus, these reactive structures are much less stable than inappropriately oriented protonated dimers (67–40 kJ mol^{-1} energy differences for POM with different central atoms (Table 4)) because of the resulting absence of electrostatic stabilization.

The rearrangement of protonated dimer D to co-adsorbed species on $H_3PW_{12}O_{40}$ showed no additional barrier above the energy difference between the two intermediates (Supporting information). The activation barrier to form DME from co-adsorbed species (75 kJ mol^{-1} on $H_3PW_{12}O_{40}$; Table 4) is much larger than the barrier to form protonated dimers (<1 kJ mol^{-1} on $H_3PW_{12}O_{40}$); as a result, co-adsorbed species invariably rearrange to protonated dimers before forming DME. Co-adsorbed species merely represent a small "ledge" along the reaction coordinate that connects protonated dimers to DME formation transition states; these co-adsorbed species avoid the configurational hurdles imposed by inappropriate atomic orientations in protonated dimers. The rapid interconversion of protonated dimers and co-adsorbed species (relative to DME formation rates) cause them to be present at thermodynamic ratios on POM clusters; thus, protonated dimers are much more abundant than co-adsorbed species (by $\sim 10^8$ at 433 K) because of their greater stability (Table 4). These protonated dimers convert via their sequential rearrangement to properly oriented co-adsorbed species and then DME formation transition states; thus, measured activation barriers for the direct route reflect energy differences between these dimers and DME formation transition states.

Direct methyl transfer between two adsorbed CH_3OH molecules proceeds via a transition state (TS3 in Fig. 3b) that forms DME and H_2O simultaneously (Scheme 2, Step 4). This reaction is an S_N2 substitution in which CH_3OH displaces H_2O at the electrophilic carbon in the methyl group. The proton is transferred to the CH_3OH monomer (H_{C1}–O_{C1} = 0.188 nm; H_{C1}–O_{M1} = 0.099 nm; Table 3) and the C–O bond is cleaved at the transition state, forming a planar methyl cation located between H_2O and CH_3OH molecules. The methyl C-atom is nearly equidistant between the O-atoms of H_2O (C_{M1}–O_{M1} = 0.193 nm) and CH_3OH (C_{M1}–O_{M2} = 0.201 nm); these two molecules decrease the methyl charge (from +0.90 e to +0.56 e Bader charge) by delocalizing it (+0.18 e and +0.17 e Bader charges on CH_3OH and H_2O, respectively), while the conjugate base (vicinal O-atoms (O_{C2} and O_{C1}) in the POM) stabilizes these positive charges via electrostatic interactions. The methyl C-atom (C_{M1}), the H_2O O-atom (O_{M1}), and the CH_3OH O-atom (O_{M2}) lie along a line at the direct transition state for all central atoms including $H_6CoW_{12}O_{40}$, in contrast to the sequential transition states. This is because the organic cation is more stable (relative to smaller ones at both of the sequential transition states) and because the linear structures required for S_N2 reactions do not require significant separations of the cation and conjugate anion. The energy of this transition state is −14 kJ mol^{-1} on $H_3PW_{12}O_{40}$, relative to two gas-phase CH_3OH; it increases as acids weaken (Fig. 5a) because of the increasing energy cost of separating charges to form ion-pairs. The energy of the direct transition state is much lower than for either of the two transition states in the sequential dehydration route (Scheme 3; 69 kJ mol^{-1} and 51 kJ mol^{-1} for TS1 and TS2 on $H_3PW_{12}O_{40}$). These differences predominantly reflect ion–dipole interactions between the methyl and an additional O-atom, which significantly stabilize the direct transition state. Blaszkowski and van Santen calculated a direct DME formation transition state energy (15 kJ mol^{-1} relative to the gas-phase reactants) that lies within the range of the POM clusters and also had an energy that was significantly lower than that of the sequential route (140 kJ mol^{-1} relative to the gas-phase reactants) [34]. The activation barrier for direct DME formation (TS3), measured with respect to its protonated dimer precursor, is much higher than the corresponding energy relative to gas-phase CH_3OH (141 kJ mol^{-1} on $H_3PW_{12}O_{40}$; Fig. 6b) because the formation of protonated dimers (from two gas-phase CH_3OH) is quite exothermic (−155 kJ mol^{-1} on $H_3PW_{12}O_{40}$; Fig. 4). Catalytic dehydration turnovers are completed by the sequential desorption of H_2O and DME and the re-protonation of the POM cluster (Scheme 2, Step 5) and have combined desorption energies of 94–103 kJ mol^{-1} (Table 4).

Significantly lower energies (relative to gas-phase CH_3OH) for the direct transition state, compared to those for the sequential transition states (Fig. 5a and Scheme 3), and the very exothermic adsorption of two CH_3OH to form protonated dimers (Fig. 4) indicate the importance of solvating unstable cations in CH_3OH dehydration reactions (Fig. 5a). These interactions have been examined among gas-phase cations and H_2O, alkanols, amines or pyridines [51–53] to probe the solvation of cations in condensed media. The stability of H^+ [51,53] increases monotonically, but less than proportionally, as the number of solvating H_2O or CH_3OH molecules increases. The proton affinity of an isolated CH_3OH is −754 kJ mol^{-1} [54], while the proton affinity of two CH_3OH to form a dimer is −890 kJ mol^{-1} (see Supporting information). These large differences in stability between $[CH_3OH_2]^+$ and $[(CH_3OH)_2H]^+$ cause the latter, but not the former, to exist as protonated species in con-

tact with POM clusters. The stability gained by solvating a proton between two CH_3OH favors protonated dimers over co-adsorbed species. This additional stability favors high coverages of protonated dimers during catalysis and renders co-adsorbed structures as kinetically-irrelevant minority species. Adsorption of a third CH_3OH molecule near protonated dimers creates CH_3OH trimers, which facilitate DME formation without high energy reorientation (calculation details for $H_3PW_{12}O_{40}$ in Supporting information), similar to co-adsorbed species, but do not further solvate the protons. Surface concentrations of trimers are negligible at reaction conditions because the incremental stability from a third CH_3OH (-20 kJ mol^{-1} relative to a protonated dimer and gas-phase CH_3OH) does not offset the large entropy penalty involved in the adsorption step. Thus, CH_3OH trimers do not contribute to measured rates, in spite of their lower activation barriers for DME formation.

3.4. Relative contributions of sequential and direct routes in the dehydration of methanol to dimethyl ether

Next, we examine the rate equations for sequential and direct routes to determine their respective contributions to CH_3OH dehydration rates and to interpret the chemical significance of the kinetic parameters (α and β; Eq. (3)) measured from rate data (Fig. 1a). Their relative contributions are determined from rate and equilibrium constants estimated from DFT-derived energies for intermediates and transition states in sequential (Scheme 1) and direct (Scheme 2) routes, taken together with statistical mechanics treatments of activation and reaction entropies [55] (details in Supporting information). Estimates for rate and equilibrium constants are reported here at the temperature used to measure most of the rate data (433 K; Fig. 8).

The rate equation for the sequential route (Eq. (4)) considers only methoxide and monomer species as surface intermediates, but neglects protonated dimers (Scheme 2). The effective stabilization of dimer structures caused by electrostatic interactions (Section 3.3.3), however, leads to a significant presence of these species during CH_3OH dehydration catalysis. These protonated dimers are in quasi-equilibrium with monomers (and a gas-phase CH_3OH molecule) because of rapid CH_3OH adsorption–desorption steps; equilibrium constant estimates for dimer formation (4×10^3 kPa^{-1} to 1×10^6 kPa^{-1}) at 433 K for all Keggin compositions) indicate that dimers are present at substantial concentrations over all CH_3OH pressures. Thus, contributions from protonated dimers must be included in the site balance of the sequential rate expression, as we describe next.

CH_3OH dehydration rates via sequential pathways, including contributions from protonated dimers, are given by (derivation in Supporting information):

$$\frac{r_s}{[H^+]} = \frac{k_{DME,s}K_P(CH_3OH)}{1 + \frac{k_{DME,s}}{k_{elim}}K_P(CH_3OH) + \frac{k_{DME,s}}{k_{elim}}K_PK_D(CH_3OH)^2} \quad (7)$$

in which rate and equilibrium constants are defined for the elementary steps in Schemes 1 and 2. Significant dimer coverages (reflected in the magnitude of the third term in the denominator of Eq. (7) relative to the others) would cause a negative rate dependence at high CH_3OH pressures, as found at lower temperatures (343–373 K) in 2-butanol dehydration reactions, for which the kinetically-relevant step is also the elimination of H_2O from monomers that compete for protons with unreactive dimers [2,48]. At pressures up to 20 kPa, CH_3OH dehydration rates did not decrease with increasing CH_3OH pressure, an observation that seems inconsistent with Eq. (7), given the large equilibrium constants for dimer formation (K_D). We consider this indirect evidence for the lack of involvement of sequential routes in CH_3OH dehydration catalysis, a conclusion confirmed by detailed comparisons of theory and experiment discussed below.

Next, we discuss the contributions of direct and sequential pathways in the context of ratios of their rates using estimates for their respective kinetic and thermodynamic constants (derivations and calculations in Supporting information). Rate ratios for the sequential (r_s) and direct (r_d) routes are given by:

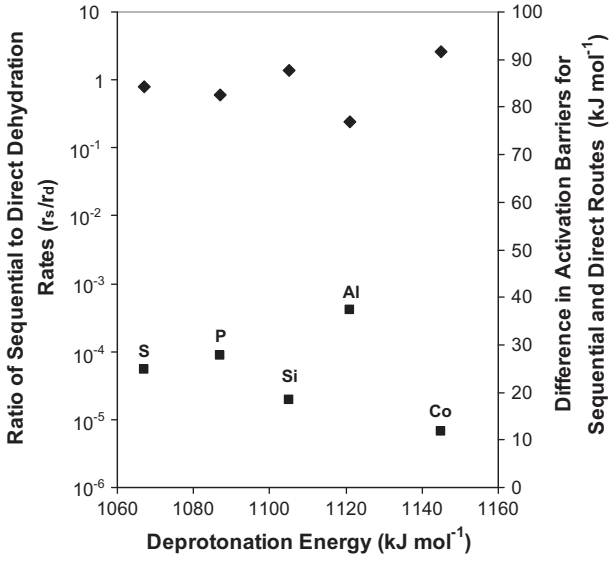

Fig. 7. Comparisons of sequential and direct route contributions to CH_3OH dehydration as ratios of rates (■) and differences in activation barriers (♦) for Keggin clusters with different central atoms (S, P, Si, Al, Co). Predicted ratios of sequential to direct dehydration rates (0.01 kPa CH_3OH) were calculated from Eq. (8), with rate and equilibrium constants estimated from DFT-derived energies of intermediates and transition states and statistical descriptions of entropy. Ratios are far below unity for all Keggin catalysts. Activation barriers for the sequential route were calculated as H_2O elimination (TS1 in Fig. 3a) from monomers and activation barriers for the direct route were calculated as DME formation (TS3 in Fig. 3b) from a monomer and gas-phase CH_3OH. Differences in activation barriers were calculated as $E_{a,seq} - E_{a,direct}$.

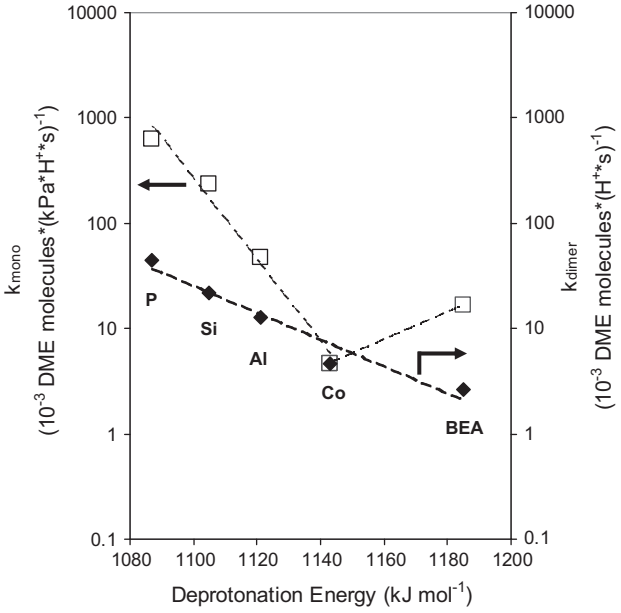

Fig. 8. Measured first-order rate constants (k_{mono}, □; Eq. (9)) and zero-order rate constants (k_{dimer}, ♦; Eq. (10)) of CH_3OH dehydration to DME (433 K) as a function of DPE values for $H_{8-n}X^{n+}W_{12}O_{40}/SiO_2$ (X = P, Si, Al, Co) and H-BEA.

$$\frac{r_s}{r_d} = \frac{k_{e\,lim}}{k_{DME,d}K_C K_D(CH_3OH)} \quad (8)$$

in which all terms correspond to the elementary steps in Schemes 1 and 2. The rate constant for H_2O elimination from monomers (k_{elim} in Eq. (8) and Scheme 1) reflects the difference in free energy between the sequential H_2O elimination transition state (TS1 in Fig. 3a) and the adsorbed CH_3OH monomer (A in Fig. 3a). The product $k_{DME,S}K_CK_D$ in the denominator of Eq. (8) reflects the difference in free energy between the DME formation transition state in the direct route (TS3 in Fig. 3b) and the free energy of an adsorbed CH_3OH monomer and a gas-phase CH_3OH. The ratio of the rate constants in Eq. (8) merely reflects the free energy difference between the two relevant transition states (TS1 and TS3 in Fig. 3). These rate ratios range from 6.6×10^{-6} to 4.1×10^{-4} on all POM clusters at 433 K and 0.01 kPa CH_3OH (Fig. 7), which are the most favorable conditions for sequential routes. Direct routes are favored even more at the higher CH_3OH pressures required for practical turnover rates (e.g. >0.5 kPa CH_3OH needed to reach the highest rates; Fig. 1a). Rate ratio predictions indicate that temperatures well above 700 K are required for detectable contributions from sequential routes, at which point CH_3OH dehydration equilibrium renders the dynamics of this reaction irrelevant and CH_3OH-DME homologation reactions would prevail. As a result, we conclude that CH_3OH dehydration proceeds exclusively via direct routes at all conditions used on Keggin clusters.

Free energy differences between the transition states for H_2O elimination and direct DME formation determine the relative contributions of direct and sequential routes on the various POM clusters. Activation entropies and the "molecularity" of a given transition state are similar on all POM clusters because of their similar structures [9]; thus, free energy differences reflect the corresponding differences in transition state energies among these catalysts. This is consistent with the results in Fig. 7, where differences in activation barriers of H_2O elimination and direct DME formation (referred in both instances to an adsorbed monomer and a gas-phase CH_3OH molecule) show the opposite dependence on DPE as the ratios of rates via the sequential and direct routes. Activation barriers for the sequential route are 77–92 kJ mol^{-1} larger than for the direct route on these POM clusters (Fig. 7), and this energetic preference of the direct route reflects the stabilization of the methyl cation at its transition state by both H_2O and CH_3OH (Fig. 3b and Scheme 3). The effect of DPE on the differences in activation barriers between the two routes is small (15 kJ mol^{-1} for these clusters; Fig. 7), however, it causes significant changes in rate ratios as a result of the exponential effects of activation barriers. We do not anticipate that rate ratios will increase above 4×10^{-4} (shown for $H_5AlW_{12}O_{40}$ in Fig. 7) in the DPE range available in solid acids (1087 kJ mol^{-1} for $H_3PW_{12}O_{40}$ to 1200 kJ mol^{-1} for zeolites [3]). Contributions from the sequential route become smaller for acids stronger than $H_5AlW_{12}O_{40}$ because charges in the direct transition state (+0.91 e Bader charge at TS3) are larger and more delocalized than for the sequential H_2O elimination transition state (+0.76 e Bader charge at TS1); as a result, transition state energies for the direct route (TS3) decrease with increasing acid strength more than for the sequential H_2O elimination counterpart (Fig. 5a). The expected contributions from sequential pathways also decrease for acids weaker than $H_5AlW_{12}O_{40}$ because their earlier H_2O elimination transition states (shown in Fig. 6 for $H_6CoW_{12}O_{40}$; Section 3.3.2) lead to activation barriers larger than expected based on the effects of DPE found on the other POM compositions (Fig. 5b).

We also anticipate that DME formation by direct routes will be favored to an even greater extent on zeolites than on POM clusters because of the preferential stabilization of the direct transition states via van der Waals forces within the constrained environments provided by zeolites. Van der Waals forces preferentially stabilize direct DME formation transition states over sequential H_2O elimination transition states because of the larger number of van der Waal contacts introduced by the additional CH_3OH molecule in direct transition states. When spatial constraints favor the smaller transition state in the sequential route (e.g. small-pore zeolites), they do so by inhibition of the facile direct reactions, making these materials much less reactive in CH_3OH dehydration catalysis. Thus, we conclude that the direct route dominates CH_3OH dehydration over the entire range of acid strengths and reaction conditions relevant to solid acids.

For CH_3OH dehydration by the direct route, the chemical origins of measured kinetic parameters (α and β in Eq. (3)) can be interpreted by comparison to the rate equation for these elementary steps (Eq. (5); Scheme 2). The apparent first-order rate constant measured at low CH_3OH pressures (i.e. $\alpha \equiv k_{mono}$) reflects the free energy change between the DME transition state (TS 3 in Fig. 3b) and a monomer and a gas-phase CH_3OH molecule:

$$k_{mono} = k_{DME,D}K_CK_D = e^{-(\Delta G^{\ddagger} - \Delta G_{monomer} - \Delta G_{CH_3OH})/RT} \quad (9)$$

At high CH_3OH pressures, measured zero-order rate constants (i.e. $\alpha/\beta \equiv k_{dimer}$) reflect the free energy required to form the DME transition state from protonated dimers:

$$k_{dimer} = k_{DME,D}K_C = e^{-(\Delta G^{\ddagger} - \Delta G_{dimer})/RT} \quad (10)$$

Estimated values of k_{mono} and k_{dimer}, calculated from DFT energies and transition state theory, are 50 (kPa s)$^{-1}$ and 1×10^{-4} s^{-1}, respectively, on $H_3PW_{12}O_{40}$ at 433 K (calculations included in Supporting information). These values are in reasonable agreement with measured apparent rate constants (k_{mono} = 0.62 (kPa s)$^{-1}$ and $k_{dimer} = 4.5 \times 10^{-2}$ s^{-1}), especially in view of the approximate nature of the theoretical treatments. Theoretical and measured rate constants are also in reasonable agreement for other Keggin clusters; on $H_6CoW_{12}O_{40}$, the weakest acid, measured k_{mono} and k_{dimer} values are 4.7×10^{-3} (kPa s)$^{-1}$ and 4.7×10^{-3} s^{-1} (433 K) and estimated values are 1 (kPa s)$^{-1}$ and 3×10^{-4} s^{-1}. We confirm with these comparisons that CH_3OH dehydration proceeds via direct routes on POM clusters at temperatures and pressures relevant for its catalytic practice.

3.5. Effects of composition and deprotonation energies on methanol dehydration turnover rates on solid acids

Measured rates, accurately described by Eq. (3), taken together with theoretical treatments of the direct and sequential dehydration routes (Sections 3.3 and 3.4) indicate that the direct route is responsible for the formation of DME on POM clusters. As a result, measured first-order (k_{mono}) and zero-order (k_{dimer}) rate constants reflect the free energy of the transition state for these direct pathways (TS3) relative to CH_3OH monomers (A in Fig. 3a) and protonated dimers (D and E in Fig. 3b), respectively.

Fig. 8 shows measured k_{mono} and k_{dimer} values at 433 K (obtained by regressing data to the form of Eq. (3)) as a function of DPE estimates for Keggin POM clusters with P, Si, Al, and Co central atoms and zeolite H-BEA. Both rate constants decreased exponentially with increasing DPE (decreasing acid strength) for Keggin POM clusters, as also found for the rate constants involved in alkanol elimination and alkene isomerization [9,48]. These exponential effects are consistent with the predominant effects of DPE on the energies (instead of the entropies) of intermediates and transition states, whose molecular structures remain similar for all POM clusters. When DPE predominantly influences activation energies, these sensitivities of rate constants can be expressed in terms of the corresponding effects of DPE on measured activation energies [9]:

$$\frac{d(\ln k)}{d(\mathrm{DPE})} = -\frac{1}{\mathrm{RT}}\frac{d(E_a)}{d(\mathrm{DPE})} \tag{11}$$

The effects of DPE on k_{mono} and k_{dimer} (Fig. 8) indicate that apparent activation energies increase as acids weaken (DPE increases). The sensitivity of k_{mono} to DPE (−0.093 slope, Fig. 8, 433 K) is greater than for k_{dimer} (−0.028 slope) and indicates that activation energies for the term k_{mono} are more sensitive to acid strength than for the term k_{dimer}. On H-BEA, k_{dimer} lies along the trend defined by the POM clusters, but k_{mono} is ~100 times larger. This discrepancy in k_{mono} reflects van der Waals contributions, relevant only to k_{mono} because they affect the transition state and adsorbed CH_3OH monomers to different extents, as discussed later in this section.

These trends are consistent with thermochemical cycles that use convenient hypothetical paths to a given transition state structure by exploiting the path independence of free energies, as used previously to describe adsorption in zeolites [56] and the effects of DPE and acid strength in acid catalysis [9,48,49]. In this context, activation energies for steps involving late ion-pair transition states (E_a) depend on the DPE of the acid, the proton affinity of gas-phase reactants (ΔE_{prot}), the interaction energy between the transition state and conjugate base (E_{int}) and the adsorption energy of reactants (ΔE_{ads}, relative to their gas-phase analogs) involved in the formation of the transition state (e.g., CH_3OH monomer for k_{mono}; protonated dimer for k_{dimer}):

$$E_a = \mathrm{DPE} + \Delta E_{prot} + E_{int} - \Delta E_{ads} \tag{12}$$

The thermochemical cycles for k_{mono} and k_{dimer} (Scheme 4) relate the DME formation transition state (TS3) to the monomer and protonated dimer, respectively. ΔE_{prot} is the energy required to add a free proton to two gas-phase CH_3OH molecules to form the gas-phase analog of the transition state (Scheme 3). The unstable character of free protons makes these reactions very exothermic, but these energies can be estimated from experiment or DFT calculations [51,52,54]. The protonation of two CH_3OH molecules to form a methyl cation located between the O-atoms in H_2O and CH_3OH (TS3 in Fig. 3b) gives a ΔE_{prot} value (−693 kJ mol^{-1}), which is much more negative than for the formation of the interacting methyl and H_2O species (−558 kJ mol^{-1}) involved in H_2O elimination to form methoxides (TS1 in Fig. 3a) or for the interacting methyl and CH_3OH species (−617 kJ mol^{-1}) involved in DME formation via methoxide/CH_3OH pairs in the sequential DME formation route (TS2 in Fig. 3a) (details of gas-phase calculations are reported in Supporting information) [46,51]. Solvation of methyl cations by concerted dipole-ion interactions with H_2O and CH_3OH (−210 kJ mol^{-1}) significantly stabilize the transition state for the direct route relative to either of the two transition states in the sequential route (Scheme 3), which are solvated by one molecule, and favor the direct route as the preferred CH_3OH dehydration pathway.

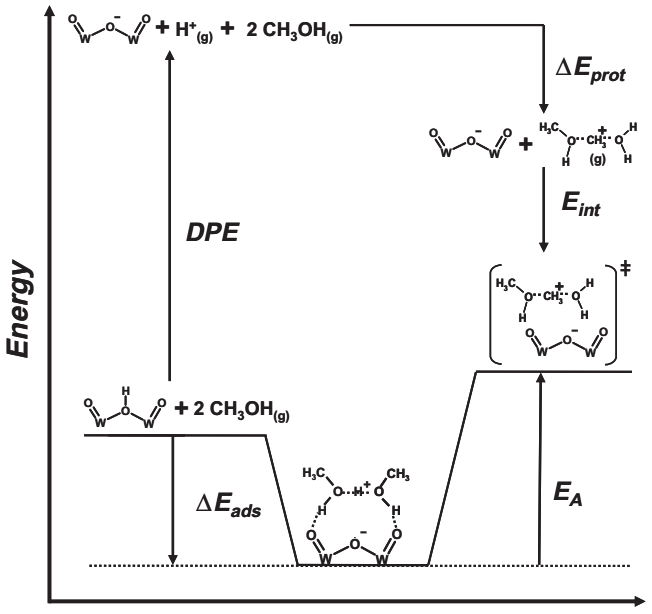

Scheme 4. Thermochemical cycle description of the activation barrier for k_{dimer} in the direct route (Scheme 2 and Eq. (12)). The activation energy (E_A) depends on the catalyst deprotonation energy (DPE), reactant proton affinity (ΔE_{prot}), transition state stabilization energy (E_{int}), and reactant adsorption energy as a protonated dimer (ΔE_{ads}).

For full ion-pairs at late transition states, E_{int} predominantly reflects electrostatic interactions [48], but also includes van der Waals forces, whose contributions become significant within constrained spaces, such as those in zeolite micropores, and H-bonding between molecules and framework O-atoms. Activation energies measured with respect to the intermediate directly preceding the transition state along the reaction coordinate, such as the case for k_{dimer}, are typically insensitive to van der Waals and H-bonding interactions, because their respective contributions to E_{int} and ΔE_{ads} tend to cancel out. In such instances, the difference in electrostatic stabilization between the adsorbed intermediate (ΔE_{ads}) and transition state (E_{int}) is the strongest determinant of the dependence of activation energies on DPE. Van der Waals and H-bonding interactions influence activation energies only when intermediates and transition states are solvated to different extents, as shown later for k_{mono} on H-BEA zeolites where van der Waals interactions are a natural consequence of confinement.

The effects of DPE on E_a reflect the individual sensitivities of each of the terms included in the thermochemical cycle for a given activation energy (Eq. (12)):

$$\frac{d(E_a)}{d(\mathrm{DPE})} = 1 + \frac{d(E_{int})}{d(\mathrm{DPE})} - \frac{d(\Delta E_{ads})}{d(\mathrm{DPE})} \tag{13}$$

The term corresponding to $d(\Delta E_{prot})/d(\mathrm{DPE})$ has been removed from Eq. (13) because ΔE_{prot} depends only on the properties of gaseous molecules. The measured values of k_{mono} and k_{dimer} (Fig. 8) together with Eq. (11) give $d(E_a)/d(\mathrm{DPE})$ values of 0.34 and 0.10, respectively, for these two rate parameters (Table 5). Both $d(E_a)/d(\mathrm{DPE})$ values are much smaller than unity, as in the case of alkanol dehydration (0.15) and alkene isomerization (0.32) on POM and H-zeolite catalysts [9,48]. These small values primarily reflect the stabilization of cationic transition states by the conjugate base ($E_{int} < 0$), which becomes stronger (more negative) as acids weaken ($d(E_{int})/d(\mathrm{DPE}) < 0$) and attenuate the effects of DPE on activation energies. Electrostatic stabilization at the transition state does not fully recover the energy required to overcome electrostatic interactions during the removal of the proton [9]. Protons are the smallest and

Table 5
Dependences of measured and calculated activation barriers on deprotonation energies ($d(E_a)/d(\mathrm{DPE})$) for Keggin polyoxometalates and zeolite BEA.

Reaction	Measured	Calculated[c]
Sequential H_2O elimination	–	0.03
Sequential DME formation	–	0.42
Direct DME formation		
From monomers	0.34[a]	0.22
From protonated dimers	0.10[a]	−0.05
Butanol elimination	0.15[b]	–
Alkane isomerization	0.32[b]	–

[a] Values taken from slopes of rate constants (at 433 K) shown in Fig. 8 and Eq. (11).
[b] Values for butanol elimination (at 373 K) and *n*-hexane isomerization (473 K) taken from Ref. [9].
[c] Values taken from slopes shown in Fig. 5b.

one of the hardest Lewis acids [57] and consequently, have the strongest electrostatic interactions with anions; thus, $d(E_{int})/d(DPE)$ values lie between 0 and −1 and approach the latter values for small and highly charged cations at transition states. Smaller cations, with shorter interaction distances and a more concentrated positive charge, recover a larger fraction of the DPE as ion-pairs and weaken the effects of acid strength on activation energies compared with larger cations with more diffuse positive charges.

The effects of DPE on transition state stabilization can be discerned from DFT-derived energies of transition states (relative to two gas-phase CH_3OH molecules and a non-interacting POM cluster) on POM clusters with different central atoms (except for the "bent" sequential transition states found on $H_6CoW_{12}O_{40}$ clusters (Fig. 6)). The energy of the transition state for direct DME formation (TS3 in Fig. 3b) increases almost linearly with increasing DPE (Fig. 5a; 0.39 slope), indicating that stronger acids favor the formation of more stable ion-pairs. As expected from Eq. (13), this slope is smaller than unity because electrostatic stabilization of protons (reflected in DPE values) and transition states (reflected in E_{int} values) both increase as acids weaken. Thus, the effects of composition on DPE are compensated by those for E_{int} and energies of transition states are attenuated to DPE. The combined Bader charges on the methyl and on the nearby stabilizing molecules for TS1 (+0.59 e and +0.20 e for the methyl and H_2O) and TS2 (+0.57 e and +0.19 e for the methyl and CH_3OH) are smaller than for TS3 (+0.56 e, +0.17 e, and +0.18 e for the methyl, H_2O, and CH_3OH); they are also less diffuse because the positive charge is delocalized over one fewer molecule at the transition state. Thus, transition state energies (relative to two gas-phase CH_3OH) for the sequential H_2O elimination (TS1) and DME formation (TS2) have slopes (0.23 and 0.25, respectively) which are smaller than that for the direct route (0.39) (Fig. 5a). Activation barriers calculated for sequential and direct routes on aluminosilicate clusters also depended weakly on acid strength [34] as a result of electrostatic interactions at the transition state that compensate for the DPE of the acid.

Next, we consider the effects of adsorption energies (Fig. 4) in determining DPE effects on activation barriers (Fig. 5b), which measure transition state energies (Fig. 5a) relative to reaction intermediates that precede them along the reaction coordinate. Activation barriers for H_2O elimination from adsorbed monomers are much less sensitive to DPE (0.03 slope; Table 5) than those for DME formation from methoxide/CH_3OH pairs (0.42 slope; Table 5) in the sequential route (Fig. 5b), even though their slopes are similar when transition state energies are measured with respect to two gas-phase CH_3OH molecules (Fig. 5a). These differences in slopes reflect the opposite effects of DPE on monomer and methoxide formation energies (Fig. 4); adsorbed monomers become less stable (0.16 slope) while methoxide/CH_3OH pairs become more stable (−0.12 slope) with increasing DPE.

The rate equation for the prevailing direct route (Section 3.4) shows that the steps responsible for measured k_{mono} and k_{dimer} values (Fig. 8) share the same DME formation transition state (TS3). Their respective activation energies, however, show different sensitivities to DPE (0.34 and 0.10 slopes, respectively) because of the contrasting effects of DPE on their respective adsorbed intermediates (monomers and protonated dimers for k_{mono} and k_{dimer}, respectively). Calculated adsorption energies (relative to gas-phase CH_3OH) for monomers (A in Fig. 3a) and protonated dimers (D and E in Fig. 3b) become less negative with increasing DPE (Fig. 4). These DPE effects are stronger for protonated dimers than monomers (slopes of 0.44 and 0.13, respectively) because monomers are less charged than dimers. The O_{C1}–H_{C1} bond distance (0.108 nm) and the Bader charge on the CH_3OH (+0.08 e) in the monomer are only slightly larger than those in non-interacting clusters (O_{C1}–H_{C1} = 0.098 nm) and CH_3OH (+0.00 e Bader charge), indicating that charge separation is not detectable upon forming the monomer, consistent with the weak effects of DPE on monomer formation energies (Fig. 4). Protonated dimers involve significant proton transfer (O_{C1}–H_{C1} = 0.139–0.158 nm), a substantial positive charge (+0.88 to +0.84 e Bader charge), and strong stabilization by the conjugate anion. As a result, dimers become less stable with the conjugate anion as DPE increases (Fig. 4).

DFT-derived activation barriers for DME formation (TS3) from adsorbed monomers (and a gas-phase CH_3OH molecule) and protonated dimers (Fig. 5b) correspond to measured activation energies for k_{mono} and k_{dimer}, respectively. The slope of the activation barriers (Table 5) for k_{mono} is larger (0.22) than that for k_{dimer} (−0.05) (Fig. 5b) and shows DPE effects on the stability of the ion-pairs at the transition state are largely offset by the effects of DPE on the stability of charged protonated dimers, but not uncharged monomers. Slopes for measured k_{mono} and k_{dimer} values (Fig. 8 and Table 5; 0.34 and 0.10, respectively) are both higher than predicted by DFT estimates, but the trends confirm that k_{dimer} values are less sensitive to DPE than k_{mono}, in spite of their common transition state, because of the different charges and DPE sensitivities for monomers and protonated dimers. The differences in slopes between measurements and theoretical estimates of activation barriers may reflect the effects of monomers and dimers that are adsorbed on the same POM during catalysis, but not in DFT calculations. The number of these co-adsorbed intermediates increases with the proton density of POM clusters and may cause systematic effects with composition that may be misinterpreted as consequences of concomitant changes in DPE with the valence of the central atom and the number of protons per cluster.

The activation energies for k_{mono} depend on DPE more strongly (0.34 slope; Fig. 8) than those for butanol dehydration rate constants (0.15 slope for both 2-butanol and 1-butanol) [9], for which elimination of H_2O from H-bonded butanols is the kinetically-relevant step and activation energies reflect the energy of late ion-pair transition states relative to adsorbed butanol. The calculated adsorption energies for 2-butanol on POM clusters (X = S, P, Si, Al) show the same sensitivity to DPE ($d(\Delta E_{ads,C_4H_9OH})/d(DPE)$=0.13) [49] as CH_3OH (0.13; Fig. 4); thus, the weaker effects of DPE on butanol activation energies (compared with those for CH_3OH) must reflect the more effective stabilization of their transition state by the POM conjugate anion (Eq. (13)). A charge analysis of the 2-butanol dehydration transition state shows a similar, but more localized charge than for the transition state in the direct CH_3OH dehydration route. For butanol, the charge resides entirely on the butyl cation (+0.85 e) without detectable delocalization onto the H_2O molecule (+0.03 e) [49]. In contrast, the charge is delocalized over the methyl, H_2O, and CH_3OH moieties (+0.56 e, +0.17 e, and +0.18 e, respectively) in the CH_3OH dehydration transition state; the strong coordination of methyl cations to H_2O and CH_3OH in CH_3OH dehydration delocalizes the charge at the transition state. The electrostatic stabilization of CH_3OH dehydration transition states by Keggin anions is less effective than for butanol dehydration transition states, thus, the formation of the ion-pair recovers a smaller fraction of the deprotonation energy and k_{mono} is more sensitive to DPE than the corresponding rate constant for butanol dehydration. Similar arguments account for the stronger sensitivity to DPE for transition state energies in the direct route (relative to gas-phase CH_3OH) compared with the two transition states involved in the sequential dehydration pathways (Fig. 5a).

Next, we consider the chemical significance of the value of k_{mono} measured on BEA, which lies well above the trend defined by the corresponding k_{mono} values on POM clusters, and of its k_{dimer} value, which in contrast with k_{mono}, lies along the trend defined by the POM clusters (Fig. 8). Brønsted acid sites in zeolites reside within channels of molecular dimensions; these small channels stabilize

adsorbed species, such as monomers and protonated dimers, and transition states via van der Waals contacts much more effectively than at surfaces of POM clusters. These van der Waals forces influence activation barriers via their ability to stabilize transition states (E_{int} in Eq. (12)) and their precursor reactants (ΔE_{ads} in Eq. (12)) to different extents. The DME transition state and its protonated dimer precursor each contain two CH_3OH molecules; as a result, van der Waals forces stabilize both to a similar extent, leading to activation barriers for k_{dimer} that do not sense the confined spaces responsible for van der Waals interactions. Therefore, the values of k_{dimer} on Keggin POM and H-BEA catalysts depend only on acid strength and are not affected by confinement in zeolite channels. In contrast, activation barriers of k_{mono} are influenced by the strength of van der Waals forces because the gas-phase CH_3OH not present in the monomer becomes stabilized within the zeolite at the transition state. The selective van der Waals stabilization of the transition state for k_{mono} leads to a smaller barrier on H-BEA than predicted by the effects of DPE for POM clusters (and to k_{mono} values about 100 larger than expected in Fig. 8). Calculated corrections for dispersive interactions stabilize CH_3OH adsorbed at a zeolite proton in H-ZSM-5 by 29 kJ mol^{-1} [58]. These interactions would increase rate constant estimates by ~4000-fold (at 433 K) and more than fully account for the observed deviation between the k_{mono} value on BEA and the trend defined by Keggin clusters. This correction over-predicts the k_{mono} value on BEA (by a factor of 40) because it does not account for the reduction in intermediate and transition state entropies that also arise as a consequence of confinement in zeolite channels. The effects of confinement in zeolites are larger for the transition state than for the monomer because two CH_3OH molecules are present at the active site at the transition state and only one CH_3OH molecule is present in the monomer intermediate (the other CH_3OH reactant is in the gas-phase). As a result, the pre-exponential factor for k_{mono} on BEA is lower than on Keggin clusters. Transition states and protonated dimers experience similar extents of confinement because two CH_3OH molecules are at the active site in each. These effects cancel in the pre-exponential factor of k_{dimer} so that it is the same on BEA and Keggin POM.

These data and theoretical treatments suggest that CH_3OH dehydration turnover rates can be used to assess the acid strength of solid acids of unknown structures, for which reliable DPE estimates are inaccessible, as we have shown previously for more complex alkene isomerization and dehydration of larger alkanols [59]. The k_{dimer} values measured on acids with unknown structure can be compared to the reactivity-DPE relation shown in Fig. 8 for acids of known structure to estimate DPE values for these solids within reaction environments. Similar assessments using measured values of k_{mono} can be applied, at least for materials lacking constrained environments of molecular dimensions, for which van der Waals effects influence the value of k_{mono}. The different effects of van der Waals forces on k_{mono} and k_{dimer} provide a powerful indicator of the extent to which confinement effects influence measured turnover rates. For instance, when measured k_{mono} values are larger than expected for the DPE values measured from k_{dimer} values on a given solid acid, we conclude that confinement effects significantly influence the reactivity of that solid acid, independently of its specific acid strength.

4. Conclusions

The effects of acid identity on CH_3OH dehydration rates are examined using theoretical assessments of acid strength (as deprotonation energies, DPE) and reaction paths, combined with rate constants measured on Keggin polyoxometalate (POM) clusters of varying central atom identity (P, Si, Al, Co) and zeolite H-BEA. Apparent first-order (k_{mono}) and zero-order (k_{dimer}) rate constants, measured from kinetic experiments and titrations of accessible protons, decrease exponentially with increasing DPE on these well-defined Brønsted acids, but with k_{mono} values depending more strongly on DPE than k_{dimer} values. These observations are consistent with the predominant effects of DPE on activation energies found in previous investigations of 2-butanol dehydration and *n*-hexene isomerization reactions. Measured rates alone are unable to ascertain the chemical significance of these rate constants and their dependences on acid strength because rate expressions based on elementary steps associated with competing direct and sequential dehydration routes both agree with rate dependences. Calculations of structures, energies, and charges of intermediates and transition states involved in these routes by density functional theory (DFT) indicate the ubiquitous involvement of ion-pairs in these and other acid-catalyzed reaction pathways. The stabilities of these ion-pairs depend on DPE sensitively because charge separations required for their formation reflect the stability of the anionic conjugate base formed during deprotonation. Mechanism-based rate expressions for direct and sequential routes and estimates of their rate and equilibrium constants from statistical treatments of entropy and DFT-derived energies indicate that CH_3OH dehydration proceeds exclusively via direct reactions of co-adsorbed CH_3OH, instead of by sequential methoxide formation and reaction with CH_3OH, for all relevant solid acids and reaction conditions. All ion-pair transition states in these paths feature unstable methyl cations interacting with the anionic conjugate base via electrostatic interactions, however, H_2O and CH_3OH molecules at direct transition states solvate methyl cations more effectively than at sequential transition states and lead to the dominant role of direct routes in CH_3OH dehydration.

Measured dependences of k_{mono} and k_{dimer} on DPE indicate their activation barriers change less than commensurate changes in DPE values in agreement with the weak dependence of all calculated transition state energies (measured relative to gas-phase CH_3OH) on DPE. These effects reflect electrostatic interactions at the transition state that partially recover the energy needed to separate the proton from the conjugate anion during deprotonation and as a result, compensate DPE. Interpretations of k_{mono} and k_{dimer} as chemical events in the direct route and thermochemical descriptions of their respective activation barriers indicate that both rate constants reflect the DME formation transition state and only differ in the identity of the reacting intermediate; k_{mono} and k_{dimer} measure this transition state from uncharged monomers and protonated dimers, respectively. Similar ion-pairs and charge distributions in protonated dimers and the transition state attenuate the effects of DPE on k_{dimer}, while the weak effects of DPE on uncharged monomers leave k_{mono} more sensitive to DPE. These results are consistent with calculated energies and charges of monomers and protonated dimers and their effects on calculated activation barriers for k_{mono} and k_{dimer}. The value of k_{dimer} on BEA agrees with Keggin predictions because confinement in zeolite channels affects protonated dimers and transition states equally, however, the selective stabilization of the transition state over monomers increases k_{mono} on BEA above the trend on Keggin clusters. This study and its analysis indicates the importance of interpreting rates by mechanism-based rate expressions, whose rate and equilibrium constants reflect the properties of their involved reacting intermediates and transition states and the dependence of these constants to acid strength can be interpreted from the changes in charge distributions among them.

Acknowledgments

The authors acknowledge David Hibbitts and Craig Plaisance for technical advice about theoretical methods. The financial support from the Chemical Sciences Division, Office of Basic Energy

Sciences, Office of Science, US Department of Energy under Grant number DE-FG02-03ER15479 and the supercomputing time from the Environmental Molecular Science Laboratory, a national scientific user facility sponsored by the Department of Energy's Office of Biological and Environmental Research and located at Pacific Northwest National Laboratory, are also gratefully acknowledged. We thank Dr. Cindy Yin (UC-Berkeley), Dr. Songhai Chai (UC-Berkeley), and Dr. Stuart L. Soled (Exxon Mobil) for the synthesis of the $H_5AlW_{12}O_{40}$ and $H_6CoW_{12}O_{40}$ samples.

Appendix A. Supplementary material

Supplementary data associated with this article can be found, in the online version, at doi:10.1016/j.jcat.2010.11.017.

References

[1] D.S. Santilli, B.C. Gates, in: G. Ertl, H. Knözinger, J. Weitkamp (Eds.), Handbook of Heterogeneous Catalysis, vol. 3, Wiley-VCH, Weinheim, 1997, p. 1123.
[2] J. Macht, M.J. Janik, M. Neurock, E. Iglesia, Angew. Chem. Int. Ed. 46 (2007) 7864.
[3] M. Brändle, J. Sauer, J. Am. Chem. Soc. 120 (1998) 1556.
[4] I.A. Koppel, P. Burk, I. Koppel, I. Leito, T. Sonoda, M. Mishima, J. Am. Chem. Soc 122 (2000) 5114.
[5] A. Zecchina, S. Bordiga, G. Spoto, D. Scarano, G. Spano, F. Geobaldo, J. Chem. Soc. Faraday Trans. 92 (1996) 4863.
[6] M. Hunger, Catal. Rev. – Sci. Eng. 39 (1997) 345.
[7] H. Karge, V. Dondur, J. Phys. Chem. 94 (1990) 765.
[8] D.T. Chen, L. Zhang, C. Yi, J.A. Dumesic, J. Catal. 146 (1994) 257.
[9] J. Macht, R.T. Carr, E. Iglesia, J. Am. Chem. Soc. 131 (2009) 6554.
[10] E.G. Derouane, J.B. Nagy, P. Dejaifve, J.H.C. van Hooff, B.P. Spekman, J.C. Védrine, C. Naccache, J. Catal. 53 (1978) 40.
[11] P. Cheung, A. Bhan, G. Sunley, E. Iglesia, Angew. Chem. Int. Ed. 45 (2006) 1617.
[12] J. Ahn, B. Temel, E. Iglesia, Angew. Chem. Int. Ed. 48 (2009) 3814.
[13] J.J. Cowan, C.L. Hill, R.S. Reiner, I.A. Weinstock, Inorg. Synth. 33 (2002) 18.
[14] L.C. Baker, T.P. McCutcheon, J. Am. Chem. Soc. 78 (1956) 4503.
[15] L.C. Baker, T.P. McCutcheon, J. Am. Chem. Soc. 72 (1950) 2374.
[16] G. Kresse, J. Hafner, Phys. Rev. B. 47 (1993) 558;
G. Kresse, J. Furthmuller, Comput. Mater. Sci. 6 (1996) 15;
G. Kresse, J. Furthmuller, Phys. Rev. B. 54 (1996) 11169.
[17] D. Vanderbilt, Phys. Rev. B 41 (1990) 7892.
[18] J.P. Perdew, J.A. Chevary, S.H. Vosko, K.A. Jackson, M.R. Pederson, D.J. Singh, C. Fiolhais, Phys. Rev. B. 46 (1992) 6671.
[19] H. Jonsson, G. Mills, K.W. Jacobsen, in: B.J. Berne, G. Coccotti, D.F. Coker (Eds.), Classical and Quantum Dynamics in Condensed Phase Simulations, Kluwer Academic, New York, 1998, p. 385.
[20] G. Henkelman, H. Jonsson, J. Chem. Phys. 111 (1999) 7010.
[21] R. Bader, Atoms in Molecules: A Quantum Theory, Oxford University Press, New York, 1990.
[22] G. Henkelman, A. Arnaldsson, H. Jonsson, Comput. Mater. Sci. 36 (2006) 354;
E. Sanville, S.D. Kenny, R. Smith, G. Henkelman, J. Comput. Chem. 28 (2007) 899.
[23] C.D. Baertsch, K.T. Komala, Y.-H. Chua, E. Iglesia, J. Catal. 205 (2002) 44.
[24] M.V. Luzgin, M.S. Kazantsev, W. Wang, A. Stepanov, J. Phys. Chem. C 113 (2009) 19639.
[25] H. Hayashi, J.B. Moffat, J. Catal. 77 (1982) 473;
J.G. Highfield, J.B. Moffat, J. Catal. 95 (1985) 108;
J.G. Highfield, J.B. Moffat, J. Catal. 98 (1986) 245.
[26] Z. Qinwei, D. Jingfa, J. Catal. 116 (1989) 298.
[27] P. Salvador, W. Kladnig, J. Chem. Soc. Faraday Trans. I 73 (1977) 1153.
[28] E.G. Derouane, P. Dejaifve, J.B. Nagy, J. Mol. Catal. 3 (1977/78) 453.
[29] Y. Ono, T. Mori, J. Chem. Soc. Faraday Trans. I 77 (1981) 2209.
[30] S.R. Blaszkowski, R.A. van Santen, J. Phys. Chem. 99 (1995) 11728.
[31] C.M. Zicovich-Wilsom, P. Viruela, A. Corma, J. Phys. Chem. 99 (1995) 13224.
[32] P.E. Sinclair, C.R.A. Catlow, J. Chem. Soc. Faraday Trans. 92 (1996) 2099.
[33] S.R. Blaszkowski, R.A. van Santen, J. Am. Chem. Soc. 118 (1996) 5152.
[34] S.R. Blaszkowski, R.A. van Santen, J. Phys. Chem. B 101 (1997) 2292.
[35] M.J. Janik, R.J. Davis, M. Neurock, J. Am. Chem. Soc. 127 (2005) 5238.
[36] M. Anderson, J. Klinowski, J. Am. Chem. Soc. 112 (1990) 10.
[37] C. Tsiao, D. Corbin, C. Dybowski, J. Am. Chem. Soc. 112 (1990) 7140.
[38] A. Ison, R.J. Gorte, J. Catal. 89 (1984) 150.
[39] G.C. Pimentel, A.L. McClellan, Annu. Rev. Phys. Chem. 22 (1971) 347.
[40] G.C. Pimentel, A.L. McClellan, The Hydrogen Bond, Freeman, San Francisco, 1960.
[41] J.S. Rowlinson, Trans. Faraday Soc. 45 (1949) 974.
[42] J.D. Lambert, Discuss. Faraday Soc. 15 (1953) 226.
[43] J.D. Lambert, G.A.H. Roberts, J.S. Rowlinson, V.J. Wilkinson, Proc. Roy. Soc. (London) 196A (1949) 113.
[44] J.D. Gale, C.R. Catlow, A.K. Cheetam, J. Chem. Soc. Chem. Commun. 31 (1991) 3083.
[45] V.I. Minkin, B.Ya. Simkin, R.M. Minyaev, Quantum Chemistry of Organic Compounds – Mechanisms of Reactions, Springer-Verlag, Berlin, 1990;
S. Shaik, H.B. Schlegel, S. Wolfe, Theoretical Aspects of Physical Organic Chemistry – The S_N2 Mechanism, John Wiley & Sons, New York, 1992;
M.N. Glukhovtsev, A. Pross, L. Radom, J. Am. Chem. Soc. 117 (1995) 2024.
[46] D.R. Stull, E.F. Westrum, G.C. Sinke, The Chemical Thermodynamics of Organic Compounds, Wiley, New York, 1987.
[47] R.A. van Santen, M. Neurock, Molecular Heterogeneous Catalysis: A Mechanistic and Computational Approach, VCH-Wiley, Inc., 2006.
[48] J. Macht, M.J. Janik, M. Neurock, E. Iglesia, J. Am. Chem. Soc. 130 (2008) 10369.
[49] M.J. Janik, J. Macht, E. Iglesia, M. Neurock, J. Phys. Chem. C 113 (2009) 1872.
[50] T.M. Miller, in: D.R. Lide (Ed.), 77th ed., CRC Handbook of Chemistry and Physics, CRC Press, Inc., Boca Raton, 1996, pp. 10-199–10-213.
[51] D.H. Aue, M.T. Bowers, Gas Phase Ion Chemistry, vol. 2, Academic Press, New York, 1979. pp. 1–51.
[52] P. Kebarle, in: M. Szwarc (Ed.), Ions and Ion Pairs in Organic Reactions, vol. 1, John Wiley & Sons, New York, 1972, pp. 27–83.
[53] P. Kebarle, R.N. Haynes, J.G. Collins, J. Am. Chem. Soc. 89 (1967) 5753.
[54] E. Hunter, S. Lias, J. Phys. Chem. Ref. Data. 27 (1998) 413.
[55] J.A. Dumesic, D.F. Rudd, L.M. Aparicio, J.E. Rekoske, A.A. Treviño, The Microkinetics of Heterogeneous Catalysis, ACS Publishing, Washington, DC, 1993.
[56] M.T. Aronson, R.J. Gorte, W.E. Farneth, J. Catal. 98 (1986) 434.
[57] P.W. Ayers, R.G. Carr, R.C. Pearson, J. Chem. Phys. 124 (2006) 194107.
[58] S. Svelle, C. Tuma, X. Rozanska, T. Kerber, J. Sauer, J. Am. Chem. Soc. 131 (2009) 816.
[59] J. Macht, R. Carr, E. Iglesia, J. Catal. 264 (2009) 54.